UNIVERSITAT POLITÈCNICA DE CATALUNYA BARCELONATECH

UPCommons

Portal del coneixement obert de la UPC

http://upcommons.upc.edu/e-prints

Aquesta és una còpia de la versió *author's final draft* d'un article publicat a la revista *Chemical Engineering Journal*

http://hdl.handle.net/2117/181365

Article publicat / Published paper:

Amani, A. [et al.]. A numerical approach for non-Newtonian two-phase flows using a conservative level-set method. *Chemical engineering journal*, 1 Abril 2020, vol. 385, p. 123896:1-123896:20. DOI: <10.1016/j.cej.2019.123896>

© <2020>. Aquesta versió està disponible sota la llicència CC-BY- NC-ND 4.0 http://creativecommons.org/licenses/by-nc-nd/4.0/

A numerical approach for non-Newtonian two-phase flows using a conservative level-set method

Ahmad Amani[a,*], Néstor Balcázar[b], Alireza Naseri[a], Joaquim Rigola[a,*]

[a] *Heat and Mass Transfer Technological Center (CTTC), Universitat Politécnica de Catalunya-Barcelona Tech((UPC), ESEIAAT, Colom 11, 08222 Terrassa (Barcelona), Spain*
[b] *Termo Fluids S.L. Avda Jacquard 97 1-E, 08222 Terrassa (Barcelona), Spain*
http://www.termofluids.com

Abstract

A finite-volume based conservative level-set method is presented to numerically solve the non-Newtonian multiphase flow problems. One set of governing equations is written for the whole domain, and different phases are treated with variable material and rheological properties. Main challenging areas of numerical simulation of multiphase non-Newtonian fluids, including tracking of the interface, mass conservation of the phases, small timestep problems encountered by non-Newtonian fluids, numerical instabilities regarding the high Weissenberg Number Problem (HWNP), instabilities encouraged by low solvent to polymer viscosity ratio in viscoelastic fluids and instabilities encountered by surface tensions are addressed and proper numerical treatments are provided in the proposed method. The numerical method is validated for different types of non-Newtonian fluids, e.g. shear-thinning, shear-thickening and viscoelastic fluids using structured and unstructured meshes. The proposed numerical solver is capable of readily adopting different constitutive models for viscoelastic fluids to different stabilization approaches. The constitutive equation is solved fully coupled with the flow equations. The method is validated for non-Newtonian single-phase flows against the analytical solution of start-up Poiseuille flow and the numerical solutions of well-known lid-driven Cavity problem. For multiphase flows, impact of a viscoelastic droplet problem, non-Newtonian droplet passing through a contraction-expansion, and Newtonian/non-Newtonian drop deformation suspended in Newtonian/non-Newtonian matrix imposed to shear flow are solved, and the results are compared with the related analytical, numerical and experimental data.

Keywords: Non-Newtonian multiphase flow, Conservative level-set method, Viscoelastic fluids,

1. Introduction

A Newtonian fluid is a fluid in which the viscous stresses emerging from its flow, are linearly proportional to the local rate of change of its deformation over time. Non-Newtonian fluid, on the other hand, does not obey this rule, and in most of the cases, its viscosity is dependent on shear-rate itself or its history. Most of the fluids found in either nature or industry are non-Newtonian, e.g. blood, proteins, slurries, polymers, suspensions, emulsions, chemical reactants etc. [1]. These types of fluids usually show many exceptional characteristics, for example, shear-thinning, shear-thickening, viscoelasticity, etc. Non-Newtonian fluids have extensive applications in a variety of fields, e.g. biochemical, food, pharmaceuticals and petrochemical industries [2].

The most common type of time-independent non-Newtonian fluids are shear-thinning (or pseudoplastic), in which their apparent viscosity decreases with increasing shear rate. The shear-thickening fluids, on the other hand, are known as fluids in which their apparent viscosity increases with the shear-rate. Because of the specific characteristics, of shear-thinning and shear-thickening fluids (STF), they are used widely in different engineering applications, e.g. energy absorbers, vibration controllers, safety protectors, pharmaceutical and food industries [3, 4, 5]

Viscoelastic fluids, however, exhibit both viscous and elastic characteristics under typical flow conditions, as encountered for instance in polymer and food processing industries. While viscous liquids strain uniformly when a stress is applied, elastic solids strain instantaneously. Consequently, viscoelastic fluids exhibit time-dependent strain, i.e. when a stress is applied, their strain approaches its equilibrium value on a time-scale which is a characteristic of the fluid [2, 6].

In many of the mentioned applications, there exists a moving interface, separating two immiscible non-Newtonian fluids. For instance, the bubble behaviour in non-Newtonian fluids has vast number of ap-

*Corresponding author
Email addresses: ahmad@cttc.upc.edu.com (Ahmad Amani), nestor@cttc.upc.edu (Néstor Balcázar), anaseri@cttc.upc.edu (Alireza Naseri), quim@cttc.upc.edu (Joaquim Rigola)

plications in diverse fields, e.g., decompression sickness, volcanic eruption, glass manufacture, metallurgy, wastewater treatment, handling and processing of fermentation broths, polymer devolatilization, bubble columns, mechanical stirrers with multiphase flows, composites processing, plastic foam processing, multiphase reactors, etc. For example in different multiphase reactors of gas-liquid, fluidized bed, trickle bed, and slurry reactors used in many biochemical applications, fluids may exhibit non-Newtonian behavior [7]. A direct consequence of this behaviour is a significant change in the characteristics of the process [8, 2]. Thus, the development of accurate numerical tools for the simulation of non-Newtonian multiphase flows is vital from both fundamental and practical points of view. Different approaches are used in literature in order to develop numerical tools to solve non-Newtonian multiphase flow problems.

In the context of Marker-And-Cell (MAC) method, Tomé et al. [9] used a MAC-finite difference (FD) approach, employing a projection method to study the non-Newtonian droplet impact problem. Oishi et al. [10] used this method to study the jet-buckling problem of viscoelastic fluids. Tome and McKee [11] proved the ability of their updated MAC method on capturing physical instabilities regarding the buckling of planar jets. Despite its flexibility and robust nature, from programming point of view, this method is quite complicated to implement and is computationally expensive especially in solution of three-dimensional cases [12].

In the context of front-tracking interface capturing method, Mukherjee and Sarkar [13, 14] used this method to study the deformation of a viscoelastic droplet in a Newtonian matrix under shear flow. Ferreira and Trierweiler [15] used this method to solve the motion of deformable bubbles in non-Newtonian fluids. They have used various Generalized Newtonian Fluid (GNF), and viscoelastic models to study the rule of matrix rheology on droplet rising problem. Aggarwal and Sarkar [16] used this approach to study the deformation of a Newtonian/viscoelastic droplet suspended in a viscoelastic matrix applied to shear flow. They elaborately studied the elastic and viscous stresses at the interface, polymer orientation, and the elastic and viscous forces in the solution domain to investigate their effect on droplet deformation. Izbassarov and Muradoglu [17] used a finite-difference/front-tracking method to study an axisymmetric sudden contraction and expansion problem. In the front-tracking method, a stationary Eulerian grid is used for the fluid flow

while the interface is tracked explicitly by a separate Lagrangian grid. Despite its high accuracy, due to the required dynamic re-meshing of the Lagrangian interface mesh, this method is quite complex to implement [18].

In the context of Smoothed Particle Hydrodynamics (SPH) method, Fang et al. [19], Jiang et al. [20] and Rafiee et al. [21] used this technique to study the impacting problem of a viscoelastic droplet on a surface and also the buckling problem of a viscoelastic jet. Zainali et al. [22] presented an incompressible SPH method with an improved interface treatment procedure enabling them to model multiphase flow problems with the density and viscosity ratios up to 1000 and 100 respectively. SPH method is capable of accurately solving convection dominated flows and large deformation problems including free surfaces, without the need of any form of explicit interface tracking [19]. However, there are disadvantages regarding difficulties of including artificial viscosity, particles clustering, tensile instability, artificial stress, and boundary conditions.

In the context of lattice Boltzmann method (LBM), Wagner et al. [23] developed a new LBM to solve two-phase flow of viscoelastic liquid mixtures. They used this new approach to simulate a bubble rising in a viscoelastic fluid and were able to reproduce the experimentally observed cusp shape at the trailing end of the bubble. Frank et al. [24] presented a multiscale approach to describe the dynamics of a chain of bubbles rising in non-Newtonian fluids using the particle image velocimetry (PIV) and the LBM simulations. Wang et al. [25] presented a multiple-relaxation-time colour-gradient lattice Boltzmann model and used it to solve the deformation and breakup of a confined droplet in shear flow with power-law rheology. It was demonstrated that their model could accurately solve power-law fluids with a broad range of indices. Gupta and Sbragaglia [26] used a numerical approach based on a combination of LBM and FD schemes to study the break-up of Newtonian/viscoelastic droplets in a viscoelastic/Newtonian matrix imposed to confined shear flow. Sun et al. [27] used a LBM to study the non-Newtonian flow effects on the internal mixing subsequent to coalescence of initially stationary droplets. LBM benefits from good locality and simplicity, making it suitable for parallel computing, therefore it has attracted increasing attention in CFD simulations [28]. However, in the context of multiphase flows, due to the challenges in dealing with the sharp density transition across the interface, many of LBM models suffer from the small density-ratio limit. There are

attempts to eliminate these limits, however, due to the added differential schemes, the efficiency of the proposed models is in question [29, 28]. Also according to Zou et al. [30], there are difficulties regarding incorporation of the viscoelastic stress in LBM.

In the context of volume of fluid (VOF) method, Lunkad et al. [31] used this approach to study the viscoelastic droplet impact problem over horizontal and inclined surfaces. Favero et al. [32] used this method embedded in OpenFoam package to study internal viscoelastic multiphase flow problems. Bonito et al. [33] used a projection method to study the die-swell problem. Sun et al. [34] used this method to study the minimum in-line coalescence height of bubbles generated from a submerged nozzle in Carboxymethyl cellulose sodium (CMC) non-Newtonian aqueous solution. Torkkeli [35] used this approach to solve the dynamics of multiple horizontal bubbles rising from different orifice arrangements in a shear-thinning matrix employing a power-law GNF model. Moraga et al. [36] investigated the dam break problems of non-Newtonian fluids with applications in the sudden collapse of mine tailings, snow avalanches, debris and lava flows, and casting solidification by adopting a Carreau-Yasuda model [37]. Premlata et al. [38] used this model to study the dynamics of an air bubble rising in a non-Newtonian shear-thinning/shear-thickening matrix. Focke and Bothe [39] adopted an extended VOF method to investigate the binary droplet collisions at high Weber numbers. Abishek et al. [40] used the VOF method imbedded in OpenFOAM package to study the dynamics of a Taylor bubble in the steady and pulsatile co-current flow of Newtonian and shear-thinning liquids in a vertical tube. Araújo et al. [41] employed this method to investigate the Taylor bubbles rising through flowing non-Newtonian inelastic fluids. Figueiredo et al. [42] used a generic kernel-conformation tensor transformation to study the problem of a rotating rod in a viscoelastic fluid. López-Herrera et al. [43] used an adaptive solver to the study of the splashing of weakly viscoelastic droplets. According to Sussman and Puckett [44], an advantage of VOF method is the ability to use accurate algorithms to advect the interface, leading to accurate conservation of the mass in phases while still maintaining a sharp representation of the interfaces. However a disadvantage of the VOF method is the difficulty in computing accurate curvatures from the volume fraction function as it presents a step discontinuity.

In the context of Level-set method (LSM), Yu et al. [45] used a LSM based finite difference algorithm

to solve viscoelastic ink ejection problem coupled with an equivalent circuit model to calculate the inflow pressure. Tezduyar et al. [46] used a Convected LSM to study the viscoelastic fluid buckling problem. Prieto [47] presented a particle LSM implemented using the Finite Element Method (FEM) and semi-Lagrangian schemes to perform stochastic, micro-macro simulations of droplets rising in non-Newtonian fluids. Pillapakkam et al. [48] used a finite-element solver based on the LSM to perform direct numerical simulations (DNS) of the transient and steady-state motion of bubbles rising in a viscoelastic matrix. Their report depicted a more clear image on volume jump discontinuity phenomena in viscoelastic matrices. In LSM, the evolution of a signed distance function in space and time representing the interface is governed by an advection equation, combined with a special re-distancing algorithm, with the main advantage that the interface curvature can be accurately computed. However, discrete solution of transport equations in this method leads to numerical error in mass conservation of the fluid-phase.

Despite all the advances in the numerical simulation of non-Newtonian multiphase flows, this area is still a challenging topic regarding the difficulties related to the tracking of the interfaces, mass conservation of the phases, numerical instabilities regarding the high Weissenberg number problem (HWNP), instabilities encouraged by low solvent to polymer viscosity ratio in viscoelastic fluids and instabilities encountered by surface tensions. Therefore, the development of numerical methods capable of dealing with the aforementioned challenges in numerical simulations of multiphase non-Newtonian fluids is very demanding. Although previous efforts have been performed in the framework of front tracking, SPH, LBM, VOF, and standard LS methods, there are no previous works using the conservative level-set method [49, 50]. Therefore, objectives of this work are twofold: first to introduce a novel methodology to accurately solve multiphase flow problems in which the droplet and/or matrix represent non-Newtonian behaviour using the CLS method, integrated with numerical tools tackling aforementioned challenges, and second to use the implemented framework to study the influence of non-Newtonian rheology in droplet deformation. The present approach is numerically stable for High Weissenberg numbers and low solvent to polymer viscosity ratios. In the present CLS method, interface normals are computed using a least-squares method on a wide and symmetric nodes-stencil around the vertexes of the current cell [50]. These normals are then used for an accurate computation of

surface tension, without additional reconstruction of the distance function, as in geometrical volume-of-fluid/level-set methods [51] or fast-marching methods. Moreover, most of the computational operations are local, which permit an efficient implementation on parallel platforms. This method is designed for general unstructured meshes [50]. Indeed, the grid can be adapted to any domain, enabling for an efficient mesh distribution in regions where interface resolution has to be maximized, which is difficult by using structured grids. Furthermore, TVD flux-limiter schemes [50] are used to discretize convective terms, avoiding numerical oscillations around discontinuities, whereas the numerical diffusion is minimized. Finally, the present finite-volume formulation is attractive due to the satisfaction of the integral forms of the conservation laws over the entire domain.

The rest of the paper is organized as follows: mathematical formulations are presented in section 2, numerical discretization of governing equations are described in section 3. Special considered treatments for the main challenges of small time-step of the simulation encountered by non-Newtonian fluids, high Weissenberg number problem (HWNP), singularities of non-viscoelastic regions and low viscosity ratio problem (LVRP) are provided in sections 3.1, 3.2, 3.3 and 3.4, respectively. Numerical experiments and discussion are reported in section 4 and at the end, conclusion remarks are discussed in section 5.

2. Mathematical formulation

Navier-Stokes equations are used to describe the conservation of mass and momentum of two incompressible immiscible fluids on a spacial domain Ω with boundary $\partial\Omega$ as following [50, 52, 53]:

$$\frac{\partial}{\partial t}(\rho\mathbf{v}) + \nabla\cdot(\rho\mathbf{v}\mathbf{v}) = -\nabla p + \nabla\cdot\tau + \rho\mathbf{g} + \sigma\kappa\mathbf{n}\delta_\Gamma \text{ in } \Omega \quad (1)$$

$$\nabla\cdot\mathbf{v} = 0 \text{ in } \Omega \quad (2)$$

where ρ is density of the fluid, $\mathbf{v}$ is the velocity field, p is the pressure field, $\mathbf{g}$ is the gravitational acceleration, τ is the stress response to the deformation of the fluid, δ_Γ is the Dirac delta function concentrated at the interface (Γ), $\mathbf{n}$ is the unit normal vector outward to interface, κ is the interface curvature and σ is the

interface tension coefficient. In this formulation, the stress response τ is decomposed with the solvent-polymer stress splitting technique into a purely viscous term of τ_s corresponding to the instantaneous response of the solvent, and τ_p corresponding to the polymeric contribution of stress response:

$$\tau = \tau_s + \tau_p \tag{3}$$

where the solvent part, τ_s, is defined as below [54]:

$$\tau_s = \mu_s(\dot{\gamma}) \left(\nabla \mathbf{v} + (\nabla \mathbf{v})^T \right) \tag{4}$$

In this formulation, $\mu(\dot{\gamma})$ is the apparent viscosity of the fluids described in the context of generalized Newtonian fluid (**GNF**) models, with $\dot{\gamma}$ as shear-rate tensor of the fluid defined as:

$$\dot{\gamma} = \nabla \mathbf{v} + (\nabla \mathbf{v})^T \tag{5}$$

In this paper, power-law **GNF** model is used to describe the relation of apparent viscosity of μ_s with shear-rate tensor of $\dot{\gamma}$ as below:

$$\mu_s(\dot{\gamma}) = K|\dot{\gamma}|^{m-1} \tag{6}$$

where $|\dot{\gamma}|$ is magnitude of the shear-rate tensor outlined as $|\dot{\gamma}| = \sqrt{(\dot{\gamma} : \dot{\gamma})/2}$, K is the consistency constant and m is the power-law index. The power-law **GNF** model is able to describe *shear-thinning* (pseudo-plastic) behaviour for $m < 1$, *shear-thickening* (Dilatant) behaviour for $m > 1$ and Newtonian behaviour for $m = 1$.

The polymeric stress tensor of equation 3 is written as:

$$\tau_p = \frac{\mu_p}{\lambda_1} f_s(c) \tag{7}$$

where λ_1 is the relaxation time of the viscoelastic fluid, μ_p is the polymeric viscosity, $f_s(c)$ is a strain

Constitutive model	$f_s(\mathbf{c}) = f_r(\mathbf{c})$
Oldroyd-B	$\mathbf{c} - \mathbf{I}$
FENE-P	$\frac{L^2-3}{L^2-tr(\mathbf{c})}\mathbf{c} - \mathbf{I}$
FENE-CR	$\frac{\mathbf{c}-\mathbf{I}}{1-tr(\mathbf{c})/L^2}$

Table 1: Starin and relaxation functions of three widely used viscoelastic constitutive models.

function depending on the constitutive model and expressed in terms of the conformation tensor, $\mathbf{c}$. This tensor is an internal tensorial variable representing the macromolecular configuration of the polymeric chains. Independent of the kinetic theory, conformation tensor by definition is *symmetric positive definite* and is equal to the identity matrix $\boldsymbol{I}$ when the polymer chain is at the equilibrium. The basic mechanism for stress build-up and relaxation is governed by a differential equation of the conformation tensor and a relaxation function of $f_r(c)$ that depends on the constitutive model as follows:

$$\frac{D\boldsymbol{c}}{Dt} = \nabla\mathbf{v}^T \cdot \boldsymbol{c} + \boldsymbol{c} \cdot \nabla\mathbf{v} - \frac{1}{\lambda_1} f_r(c) \tag{8}$$

where $D\boldsymbol{c}/Dt$ is the material derivative, defined as:

$$\frac{D\boldsymbol{c}}{Dt} = \frac{\partial \boldsymbol{c}}{\partial t} + \mathbf{v} \cdot \nabla \boldsymbol{c} \tag{9}$$

Considering the incompressibility constraint (Eq. 2), this formulation could be written as:

$$\frac{D\boldsymbol{c}}{Dt} = \frac{\partial \boldsymbol{c}}{\partial t} + \nabla \cdot (\mathbf{v}\boldsymbol{c}) \tag{10}$$

The implementation of any constitutive equations is straight forward. The $f_s(c)$ and $f_r(c)$ functions of three widely used constitutive equations are defined in table 1. In this table, L is the ratio of the length of a fully extended polymer dumbbell to its equilibrium length, and $tr(c)$ is the first invarient of the conformation tensor $\boldsymbol{c}$. The summation of μ_s and μ_p of the fluid is defined as total viscosity and denoted as $\mu_0 = \mu_s + \mu_p$. The ratio of μ_s to μ_0 is defined as viscosity ratio of viscoelastic fluid also known as retardation ratio and denoted as, $\beta = \mu_s/\mu_0 \leq 1$.

The density, viscosities (μ_s and μ_p), and relaxation time can be defined as scalar-fields inside the whole domain as follows:

$$\zeta = \zeta_1 H + \zeta_2(1 - H) \tag{11}$$

where $\zeta \in \{\rho, \mu_s, \mu_p, \lambda_1\}$ and H is the Heaviside step function which takes the value one in dispersed phase and zero elsewhere.

In this research, conservative level-set (CLS) method [55], as introduced by Balcazar et al. [50] in the context of Newtonian fluids is used to track the interface. Instead of the signed distance function, d(x,t), used to represent the interface in the classical LS method, conservative LS method employs a regularized indicator function ϕ as below:

$$\phi(x,t) = \frac{1}{2}\left(tanh\left(\frac{d(x,t)}{2\varepsilon}\right) + 1\right) \tag{12}$$

where ε is the parameter that sets the thickness of the interface. ϕ varies from 0 in one fluid to 1 in other fluid. With this formulation, interface is defined by $\Gamma = \{x|\phi(x,t) = 0.5\}$.

The level-set function is advected by velocity vector field, $\mathbf{v}$, provided from solution of Navier-Stokes equations. Since the velocity field is solenoidal ($\nabla \cdot \mathbf{v} = 0$), the interface transport equation can be written in conservative form [50, 55]:

$$\frac{\partial \phi}{\partial t} + \nabla \cdot (\phi \mathbf{v}) = 0 \tag{13}$$

Since sharp changes exist in level set function at the interface, Superbee flux limiter scheme is used in discretization of the convective term in order to minimize numerical diffusion and to avoid numerical instabilities at the interface. To keep the profile and thickness of the interface constant, an additional re-initialization

equation [56, 52, 53, 50] is used:

$$\frac{\partial \phi}{\partial \tau} + \nabla \cdot \phi \left(1 - \phi\right) \mathbf{n}_{\tau=0} = \nabla \cdot \varepsilon \nabla \phi \tag{14}$$

which is advanced in pseudo-time τ. This equation consists of a compressive flux: $\phi(1-\phi)\mathbf{n}_{\tau=0}$ and a diffusion term: $\nabla \cdot \varepsilon \nabla \phi$. The first one keeps the level-set function compressed onto the interface along the normal vector $\mathbf{n}$, and the second one keeps the profile in prescribed characteristic thickness of ε. This parameter is defined based on the mesh resolution in each grid cell (P), as [50]:

$$\varepsilon_p = C_\epsilon h^{1-\alpha} \tag{15}$$

where $h = (V_P)^{1/3}$ is the grid's characteristic length with V_P as the cell's volume. The value of parameter ε in Eq. 14 at the faces is computed by linear interpolation. In all the simulations of this paper, C_ϵ is constant and equal to 0.5. parameter α, however, varies in order to change the thickness of the interface and can take values between [0,0.1], to overcome the possible numerical instabilities. Normal vector $\mathbf{n}$ on the interface and curvature κ of the interface, are obtained using [50]:

$$\mathbf{n} = \frac{\nabla \phi}{||\nabla \phi||} \tag{16}$$

$$\kappa(\phi) = -\nabla \cdot \mathbf{n} \tag{17}$$

The continuous surface force model (CSF) [57] is used for surface tension computation which converts the term $\sigma \kappa \mathbf{n} \delta_\Gamma$ in Eq. 1 to a volume force term as follows [50]:

$$\sigma \kappa \mathbf{n} \delta_\Gamma = \sigma \kappa(\phi) \nabla \phi \tag{18}$$

where $\nabla \phi$ is computed using least-square method based on vertex node stencils. By applying this approach, the explicit tracking of the interface is not necessary.

3. Numerical method

Finite-volume (FV) approach is used for the spatial discretization of transport equations on a collocated grid [50], so all the computed variables are stored at centroids of the cells, including viscoelastic constitutive equations introduced in this work. A central difference (CD) scheme is used to discretize the compressive term of re-initialization equation (14) and diffusive fluxes at the faces [53]. A distance-weighted linear interpolation is used to calculate the face values of physical properties and interface normals. A total-variation Diminishing (TVD) Superbee flux limiter is used to discretize the convective term as implemented in [50], in order to improve the numerical stability of the solver and increase the convergence of spatial discretization of the governing equations [52]. At discretized level, physical properties are regularized in the context of the CLS method. Therefore a linear average is used for density, viscosities (μ_s and μ_p) and relaxation time as $\zeta = \zeta_1\phi + \zeta_2(1-\phi)$, where $\zeta \in \{\rho, \mu_s, \mu_p, \lambda_1\}$. A classical fractional step projection method as described by [58] is used to solve the velocity-pressure coupling. In the rest of this section, the main challenges and difficulties of numerical simulations of non-Newtonian multiphase flow problems are addressed and the most prominent solution for each problem is being suggested and implemented into the solution procedure. Although none of these approaches completely solves the problem, they push the stability limits of numerical simulations of non-Newtonian flows to a higher limit.

3.1. Small time-step of the simulation

The allowable time step of the simulation is calculated by taking into account the CFL conditions on convective and diffusive terms and also by explicit treatment of surface tension. For this reason, in each cell the values of allowable times step are calculated as:

$$\Delta t_{conv} \equiv \alpha \times \left(\frac{h}{\|V_P\|} \right) \tag{19}$$

$$\Delta t_{visc} \equiv \alpha \times min\left(\frac{h^2\rho(\phi)}{\mu_p(\phi)}, \frac{h^2\rho(\phi)}{\mu_s(\phi,\dot{\gamma})} \right) \tag{20}$$

$$\Delta t_{cap} \equiv \alpha \times \left(h^{3/2} (\frac{\rho_1+\rho_2}{4\pi\sigma})^{1/2} \right) \tag{21}$$

where α is CFL coefficient. The final global value of time step is the minimum of Δt_{conv}, Δt_{visc} and Δt_{cap} in the whole domain. The difficulty of the small time-step problem arises specially in the solution of non-Newtonian shear-thinning/shear-thickening fluids, where the varying value of viscosity can increase dramatically, leading to a very small timestep resulting in huge computational costs. To circumvent this issue, diffusion term could be treated implicitly. So we suggest a second-order implicit Crank-Nicolson scheme to be used to discretize the solvent part, τ_s of the stress term τ of equation 1 where the $\mu_s(\dot{\gamma})$ can take unexpectedly high values. A second-order Adam-Bashforth scheme will be used on convective, gravity, surface tension and the polymeric part, τ_p, of the stress term τ as below:

$$\frac{\rho\mathbf{v}^* - \rho^n\mathbf{v}^n}{\Delta t} = \frac{3}{2}(R_h^v)^n - \frac{1}{2}(R_h^v)^{n-1} + \frac{1}{2}\left(\mathbf{D}_{hs}(\mathbf{v}^*) + \mathbf{D}_{hs}(\mathbf{v}^n)\right) - \nabla_h p^n \tag{22}$$

where $R_h^v = -\mathbf{C}_h(\rho\mathbf{v}) + \rho\mathbf{g} + \sigma\kappa\nabla_h(\phi) + \mathbf{D}_{hp}(\mathbf{v})$, $\mathbf{D}_{hp}(\mathbf{v}) = \nabla_h \cdot \tau_p$ and $\mathbf{D}_{hs}(\mathbf{v}) = \nabla_h \cdot \tau_s$ with $\mathbf{C}_h(\rho\mathbf{v}) = \nabla_h \cdot (\rho\mathbf{v}\mathbf{v})$ as the convective operator. In this equation, ∇_h represent the gradient operator. The spatial discretization is performed using the integral form of this equation on unstructured grids, while its time discretization leads to a system of ordinary differential equations in time. The gradients are computed at the cell centroids by a least-squares method using a stencil that includes the cell-nodes around the vertexes of the current cell. A stencil which distinguishes the neighboring points (i) of any cell (p) is used to approximate the variation of dependent variable ψ using a truncated Taylor series as used by [50], $\psi_i = \psi_p + (\mathbf{x}_i - \mathbf{x}_p) \cdot (\nabla\psi)_{\mathbf{P}}$. The application of this equation to all the points of the cell stencil results in a system of linear equations for cell $\mathbf{p}$ which its solution will conduct the value of $(\nabla\psi)_{\mathbf{P}}$. A term of pressure gradient of previous time step is added to the discretized form of equation 1. According to Armfield and Street [59] and numerical tests of Amani et al. [53], this will increase the accuracy of the momentum equation in time. A cell face volume flux as implemented by Balcazar et al. [50] is calculated using a mass conservative scheme to avoid pressure-velocity decoupling when the pressure projection is made on collocated meshes. Using this approach the fluxes conserve mass exactly. A more detailed description on

the spatial discretization of convective and diffusive terms could be found in Balcázar-Arciniega et al. [60]. Pressure-velocity coupling is solved by using a fractional-step projection method [58, 61], as follows:

- A correction to the predicted velocity applies as below, where π is the pressure correction term:

$$\frac{\rho \mathbf{v}^{n+1} - \rho \mathbf{v}^{*}}{\Delta t} = -\nabla_h \pi^{n+1} \tag{23}$$

- Poisson equation reads as follows and is solved using a preconditioned conjugated gradient method.:

$$\nabla_h \cdot \left(\frac{1}{\rho} \nabla_h (\pi^{n+1}) \right) = \frac{1}{\Delta t} \nabla_h \cdot (\mathbf{v}^{*}) \tag{24}$$

- The velocity $\mathbf{v}^{n+1}$ is corrected and pressure is update as:

$$\mathbf{v}^{n+1} = \mathbf{v}^{*} - \frac{\Delta t}{\rho} \nabla_h (\pi^{n+1}) \tag{25}$$

$$\mathbf{p}^{n+1} = \mathbf{p}^{n} + \pi^{n+1} \tag{26}$$

3.2. High Weissenberg Number Problem (HWNP)

Stiff hyperbolic nature of the constitutive equations make them prone to the numerical instabilities in numerical solution process which can lead to a blowup of the numerical values. It arises when the Weissenberg number (or equivalently the Deborah number) of the problem reaches a critical value. Weissenberg number is defined as the ratio of elastic forces to the viscous forces of the problem. It can be variously defined, but it is usually given by the relation of the value of λ_1 of the fluid and a specific characteristic time of the problem. HWNP is being linked to loss of positive definiteness of the conformation tensor [62]. This critical value varies in different problems and depends on the nature of the flow, spacial discretization and numerical algorithm. According to Fattal and Kupferman [63], Hulsen et al. [64] and Lee et al. [65], the loss of positive-definiteness of the conformation tensor is the trigger to HWNP. Moreover, according to Renardy [66], solution of viscoelastic fluids tend to have stress boundary layers with large variation in stress gradients

and exponential stress profiles near geometrical singularities. According to Fattal and Kupferman [67] and Hulsen et al. [68], under resolution of these spatial stress profiles can cause numerical instabilities as well.

Therefore, several stabilization techniques have been developed to ensure the positive-definiteness of the conformation tensor. The most prominent stabilization approaches used in the context of finite-volume method are *the positive definiteness preserving scheme* (PDPS) of Stewart et al. [69] *the square-root conformation representation* (SRCR) of Balci et al. [70] and *the log-conformation tensor representation* (LCR) of Fattal and Kupferman [63, 67]. Chen et al. [62] Provided a detailed analysis on comparison of these approaches for finite-volume simulation of viscoelastic single-phase flows regarding their implementation complexity, stability, accuracy, efficiency and applicability to complex problems.

The log-conformation representation method of Fattal and Kupferman [63, 67] is among the most robust stabilization approaches for this problem. This method uses a matrix-logarithm change of variable of conformation tensor. In addition to positive-definiteness preserving characteristic of this method, since it linearizes the exponential stress profiles, it improves the resolution of large stress gradients. In this study we use this method to deal with the HWNP. A detailed description of derivation of this method for constitutive model of form of equation 8 is presented in Appendix A. Using this method, and considering the conformation tensor equation with the form of equation 8, implementing the log-conformation representation formulation for different viscoelastic constitutive equations is straight-forward. It is merely required to specify the strain and relaxation functions of the considered constitutive equation, the rest of the solution procedure will be identical.

For regular problems with Weissenberg numbers smaller than the critical values, in order to save-up on computational costs, the standard formulation (SF) of equation 8 with a first order Euler Backward discretization approach could be used as below:

$$\boldsymbol{c}^n = \boldsymbol{c}^{n-1} + \Delta t \left[-\nabla \cdot (\mathbf{v}\boldsymbol{c}) + \nabla \mathbf{v}^T \cdot \boldsymbol{c} + \boldsymbol{c} \cdot \nabla \mathbf{v} - \frac{1}{\lambda_1} f_r(c) \right]^{n-1} \tag{27}$$

In this case, the eigendecomposition of the conformation tensor $\mathbf{c}$ will not be required and hence computa-

tional costs will be decreased while maintaining the numerical stability of the simulations.

3.3. Singularities of non-Viscoelastic regions

In the problems with viscoelastic/Newtonian interface, one-field formulation represented in section 2 leads to singularities where the value of relaxation time λ_1 is equal to zero in the Newtonian fluid causing numerical solution process to diverge. One solution to this problem would be to use the semi-analytical method (SAM) proposed by Sarkar and Schowalter [71]. Unlike the LCR approach, this method does not require any eigendecomposition and as a result imposes lower computation cost, however it does not circumvent the HWNP. In this method, the constitutive equation 8 is re-written as:

$$\lambda_1 \frac{\partial \boldsymbol{c}}{\partial t} + \boldsymbol{c} = \Xi(t) \tag{28}$$

where Ξ is:

$$\Xi = \boldsymbol{c} - f_r(c) - \lambda_1 \left(\nabla \cdot (\mathbf{v}\boldsymbol{c}) - \nabla \mathbf{v}^T \cdot \boldsymbol{c} - \boldsymbol{c} \cdot \nabla \mathbf{v} \right) \tag{29}$$

Assuming a constant Ξ during the timestep of Δt, equation 28 could be integrated in time from $t = n-1$ till $t = n$, resulting in:

$$\boldsymbol{c}^n = \boldsymbol{c}^{n-1} e^{-\Delta t/\lambda_1} + \Xi^{n-1} \left(1 - e^{-\Delta t/\lambda_1} \right) \tag{30}$$

This formulation is consistent everywhere, including non-viscoelastic fluid regions with zero relaxation time ($\lambda_1 = 0$). The disadvantage of non-circumventing the HWNP prevents this method to be used thoroughly.

Another solution for this problem would be to utilize a cut-off value in the solution process. In this method, in each iteration, cells with $\lambda_1 > \epsilon$ are being identified, and being updated to a list. The constitutive equation 8, independent of the formulation (Standard formulation or LCR) is being solved only in cells of this list.

Since SAM method does not circumvent the HWNP, and since the cut-off approach can be integrated

with LCR formulation, in this study we use the cut-off approach in order to deal with the singularities of non-viscoelastic regions in one-field formulation of governing equations. To make sure of the accuracy of the results of this method, we perform two-dimensional simulations of deformation of a droplet in a simple-shear flow with both SAM and cut-off approaches. The results are extracted and compared with reference data of Chinyoka et al. [72] for different combinations of viscoelastic/Newtonian droplet in a viscoelastic/Newtonian matrix. These results along with the simulation details are presented in Appendix B. According to these data, the results of cut-off approach is in complete agreement with the results of SAM and reference data of Chinyoka et al. [72]. Hence, in this study, the proposed cut-off approach with the value of $\epsilon = 0.005$ is being used. The results have shown to be independent of the value of ϵ, as long as $\epsilon \leq 0.005$.

3.4. Low viscosity ratio problem (LVRP)

A stability problem occurs when viscosity ratio β is relatively small. According to Amoreira and Oliveira [73], this problem causes the instabilities in numerical iterative methods to occur at lower Weissenberg numbers and impose an unbearable small timestep to the simulation. Comparing different formulations of viscoelastic fluids, Amoreira and Oliveira [73] proposed an approach named *Explicit diffusion (EDIF)*, lately known as *both-sides diffusion* (BSD) approach. Chen et al. [62] mentioned that for single-phase lid-driven cavity test case, for a small viscosity ratio of $\beta = 0.0014$, the HWNP occurs at a small Weissenberg number of 0.1, and even with different stabilization approaches of PDPS, LCR and SRCR, this problem lingers. However, Chen et al. [62] mentioned that BSD approach can lift the HWNP to almost the same critical Weissenberg numbers as possible for large viscosity ratios. As a result they believe this method (BSD) can be used along with other stabilization approaches to cope with Low viscosity ratio instability problem. In this approach the constitutive equation is not reformulated, but additional diffusion term is added and subtracted from momentum equation, one treated implicitly and the other evaluated explicitly. The implicitly treated additional diffusive term contributes to the *ellipticity* of the problem and improves the stability of the solution in cases of LVRP.

In order to analyze this problem, and since it originates in the momentum equation and not the constitutive model, we have studied the performance of different discretizations of momentum equation on providing

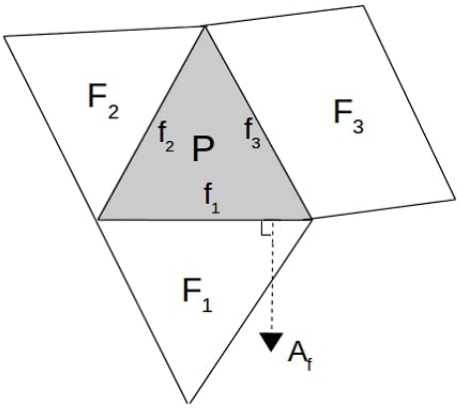

Figure 1: Control volume used to discretize equation 31.

a stable solution in the context of fractional-step projection method for a LVRP of a two-dimensional lid-driven cavity test case. Five different discretizations of Forward Euler (**FE)**, Backward Euler (**BE**), 2nd order Adams-Bashforth (**AB**), both side diffusion (**BSD**), and Semi-Implicit form as eq. 22 for predictor step of momentum equation are tested. The details of this study are provided in Appendix C. According to this test, the Semi-Implicit discretization of predictor step of momentum equation with the form of eq. 22 outperforms other methods, including BSD, and is the only method capable of solving a challenging test case of flow inside of a lid-driven cavity with viscosity ratio as low as $\beta = 0.0014$ and Weissenberg number equal to 0.75. As a result, we propose the Semi-Implicit discretization of predictor step of momentum equation with the form of eq. 22 in order to overcome the difficulties arising by low viscosity ratios (LVRP).

3.5. Spatial discretization of constitutive equation

The spatial discretization of the constitutive equation in an arbitrary cell P as shown in figure 1, in the case of either Log-conformation representation (LCR), semi-analytical method (SAM) or standard formulation (SF) of constitutive equation could be written using the integral form of transport equation taking into account the incompressibility constraint of equation 2 as below:

$$\int_{V_p} \frac{\partial \boldsymbol{\Upsilon}}{\partial t} dV = \oint_{A_p} (-\boldsymbol{\Upsilon}\mathbf{v}) \cdot d\mathbf{A} + \int_{V_p} \mathbf{S}(\Upsilon) dV \tag{31}$$

Formulation	$\boldsymbol{\Upsilon}$	$\boldsymbol{S(\Upsilon)}$
SF & SAM	c_{ij}	$\partial_k v_i c_{kj} + c_{ik}\partial_k v_j - \frac{1}{\lambda_1} f_r(c_{ij})$
LCR	Ψ_{ij}	$\Omega_{ik}\Psi_{kj} - \Psi_{ik}\Omega_{kj} + 2B_{ij} - \frac{1}{\lambda_1} G_{ik}(e^{-\Psi})_{kj}$

Table 2: Summary of the terms used in equation 31. In Cartesian tensor notation $i, j \in \{x, y, z\}$, k is dummy index $\in \{x, y, z\}$ and $\partial_k \in \{\partial/\partial x, \partial/\partial y, \partial/\partial z\}$. Tensors $\boldsymbol{\Psi}$, $\boldsymbol{\Omega}$, $\mathbf{B}$, and $\mathbf{G}$ are defined in section Appendix A.

where V_p is the volume of cell P and A_p is the relevant surface which separates two adjacent cells of P and F ($F_i \in \{F_1, F_2, ..., F_n\}$ are neighbour cells of cell P). A_p has the local area vector of d$\mathbf{A}$. Terms of $\boldsymbol{\Upsilon}$ and $\boldsymbol{S(\Upsilon)}$ related to LCR, SAM and SF are presented in table 2 . In this formulation, value of $\boldsymbol{\Upsilon}$ at the cell (face) is assumed to be constant with the value localized at the cell (face) centroids with approximation of $\boldsymbol{\Upsilon_P} = \frac{1}{V_p}\int_{V_p} \boldsymbol{\Upsilon} dV$ ($\boldsymbol{\Upsilon_f} = \frac{1}{A_p}\int_{A_p} \boldsymbol{\Upsilon} dA$).

3.6. Solution process

The solution procedure of the proposed method would be as follows. Firstly the physical properties, interface geometric properties and velocity field are initialized. Then, for the iteration time t_{n+1}, the following steps are done consecutively.

1. Allowable time step is calculated using the equations 19 and 21. To decrease the computational costs, the maximum value of α which leads to a stable simulation is used. Unless otherwise mentions, this value is 0.1.

2. The advection equation (13) is integrated in time with a 3-step third order accurate TVD Runge-Kutta scheme [74].

3. The re-initialization equation (14) is integrated in pseudo time (τ) using a third order accurate TVD Runge-Kutta scheme. The time τ is used to lead the solution into a stationary state. Since an explicit scheme is used, the time step is restricted by the viscous term of equation 14 as follows [75, 55]:

$$\Delta\tau = C_\tau min\left(\frac{h^2}{\epsilon_P}\right) \tag{32}$$

One iteration is used to solve the discretized form of equation 14. The value of C_τ in this formula serving as a CFL-like coefficient for this equation, can take values between [0.01,0.05].

4. Physical properties in the domain (density, viscosites and relaxation time) and geometrical properties at the interface (curvature and interface normal) are updated from the level-set field.

5. If applied, the list of viscoelastic regions is being updated, based on the cut-off approach described in section 3.3 .

6. The constitutive equation is integrated in time as described in equation A.11 for log-conformation representation approach or equation 27 for standard formulation approach, and the value of polymeric stress tensor at iteration time t_n are calculated.

7. The velocity and pressure fields are calculated using a fractional-step method described in section 3.1 and equations 22 through 26.

8. In order to fulfill the incompressible constraint, Eq. 2, and to avoid pressure-velocity decoupling on collocated meshes [76, 77], a cell-face velocity is used to advect the momentum and CLS function, as introduced in [75, 78].

The steps 1 to 8 are repeated to reach the desired time.

The reader is referred to [50] for further technical details on the CLS method on collocated unstructured grids. The numerical methods are implemented in an in-house parallel c++/MPI code called TermoFluids [79]. Validations and verification of the numerical methods in the context of Conservative level-set method used in this work have been reported in [52, 53, 50, 80, 81, 82, 54, 83].

4. Numerical experiments and discussion

4.1. Two-dimensional Poiseuille flow

In two dimensional Poiseuille flow test case, the flow between two infinite plates is driven by an external pressure gradient ($S = dP/dx$). Periodic boundary condition is applied in the flow direction (x), and no-slip

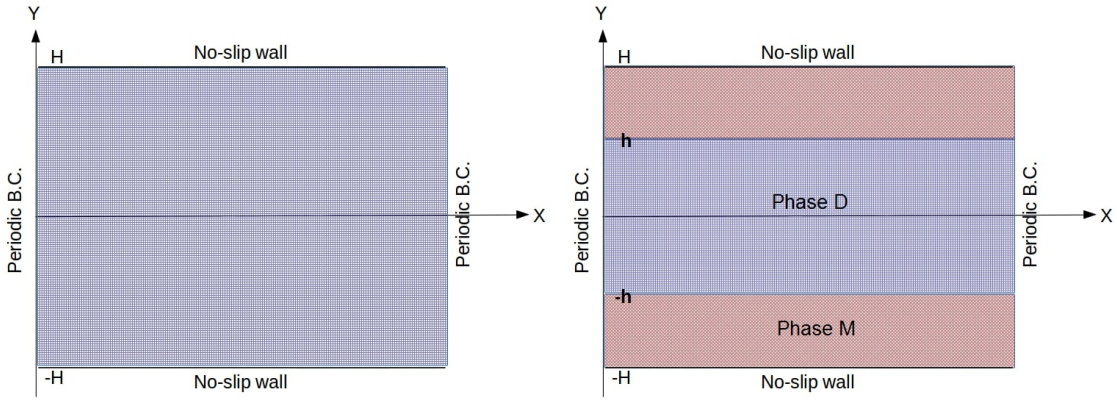

Figure 2: The schematic plot of the 2D domain of Poiseuille flow test case. Left: single-phase viscoelastic fluid problem, right: two-phase shear-thinning/shear-thickening fluids problem.

boundary condition on the walls. This problem is solved for different rheologies of viscoelastic, shear-thinning and shear-thickening fluids and the results are compared with the exact solution extracted from analytical approaches.

- For viscoelastic fluid test case, the exact solution of the transient velocity and viscoelastic stress for Oldroyd-B constitutive model exist and are presented in [84]. The geometry of the channel is presented in figure 2 left. Lengths are non-dimensionalized using the domain's height ($y^* = y/H$), velocity using characteristic velocity of $u_0 = \frac{-SH^2}{8\nu_0}$ ($u^* = u/u_0$) in which ν_0 is the total kinematic viscosity, time using $t_0 = H^2/\nu_0$ ($t^* = t/t_0$) and stress tensor using $\tau_0 = \eta u_0/H$ ($\tau^* = \tau/\tau_0$). In which variables denoted with * are dimensionless. The exact solution of the flow for this case would be as:

$$u^*(t^*, y^*) = 4y^*(1 - y^*) - 32 \sum_{n=1}^{\infty} \frac{sin(Ny^*)}{N^3} G_N(El, t^*) \tag{33}$$

where

$$G_N(El, t^*) = \begin{cases} 0.5(a_N exp(P_N t^*) + b_N exp(Q_N t)), & \beta_N^2 \geq 0 \\ exp(-\alpha_N^* t^*)(cos(\beta_N^* t^*) + \frac{S_N}{\beta_N} sin(\beta_N^* t^*)), & \beta_N^2 < 0 \end{cases} \tag{34}$$

In this formulation, the parameters are presented in table 3.

Table 3: Related parameters of equation 34

Symbol	Equation
N	$(2n-1)\pi$
El	$\lambda_1 u_0/H$
S_N	$1-17N^2El/9$
α_N	$1+N^2El/9$
β_N^2	$\alpha_N^2-4N^2El$
α_N^*	$\alpha_N/(2El)$
β_N^*	$\beta_N/(2El)$
a_N	$1+S_N/\beta_N$
b_N	$1-S_N/\beta_N$
P_N	$-\alpha_N^*+\beta_N^*$
Q_N	$-\alpha_N^*-\beta_N^*$

Using the given velocity profile, the viscoelastic stress tensor could be solved as:

$$\begin{aligned}\tau_{xx} &= 2Wi(1-\beta)(\frac{\partial u^*}{\partial y^*})^2\\ \tau_{xy} &= (1-\beta)(\frac{\partial u^*}{\partial y^*})\\ \tau_{yy} &= 0\end{aligned}$$

The initial condition is zero velocity and stress tensor in the whole domain. The numerical simulation is done in a domain with both structured and unstructured grid with the mesh size of h=H/100 until $t^*=10$. The results showed to be independent of the grid type, and were identical for structured and unstructured grids. Dimensionless numbers of Reynolds number and Weissenberg number are defined as $Re=\rho u_0 H/\nu_0$ and $Wi=\lambda_1 u_0/H$, respectively. The steady-state results of cross section velocity $u_x(y)$, along with the transient velocity at centerline and transient normal viscoelastic stress on fixed

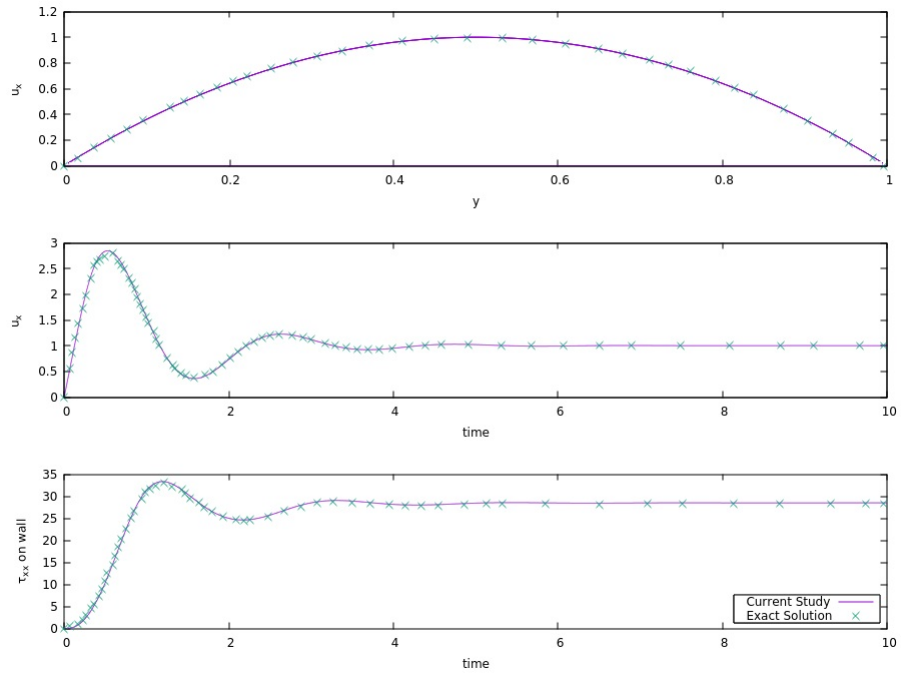

Figure 3: Numerical simulation of two-dimensional Poiseuille Oldroyd-B viscoelastic fluid flow compared with the analytical solution.

wall for a case with $\beta = 0.1$, Re=1 and Wi=1 are presented in figure 3. These results are compared with the results of exact solution where perfect agreement is seen.

- For shear-thinning, and shear-thickening rheologies, power-law GNF model is used to simulate the two-phase flow problem inside of a channel with aforementioned properties. Figure 2 right illustrates the schematic plot of the domain used for this problem with two phases called D and M. Extraction of analytical solution of this problem for power-law fluid is straight forward. The X-direction velocity profile (U) as a function of Y could be written as below:

$$U(Y) = \begin{cases} A(D)\left(h^{\frac{1+n_D}{n_D}} - |y|^{\frac{1+n_D}{n_D}}\right) + A(M)\left(H^{\frac{1+n_M}{n_M}} - h^{\frac{1+n_M}{n_M}}\right), & |y| \leq h. \\ A(M)\left(H^{\frac{1+n_M}{n_M}} - |y|^{\frac{1+n_M}{n_M}}\right), & \text{Elsewhere} \end{cases} \tag{35}$$

Case	n_D	n_M	K_D/K_M	L_1
1	1	1	1	8.23×10^{-4}
2	0.5	1	1	9.72×10^{-4}
3	0.5	1	0.5	3.25×10^{-3}
4	0.5	1	2	1.89×10^{-2}
5	1.5	1	1	9.25×10^{-4}
6	1.5	1	0.5	2.64×10^{-3}
7	1.5	1	2	4.27×10^{-3}
8	1	0.5	1	2.91×10^{-3}
9	1	0.5	0.5	4.26×10^{-3}
10	1	0.5	2	1.68×10^{-2}
11	1	1.5	1	2.49×10^{-3}
12	1	1.5	0.5	1.37×10^{-2}
13	1	1.5	2	1.84×10^{-2}

Table 4: Characteristics of cases solved for shear-thinning/shear-thickening rheological properties, along with the relative error of the numerical results, compared with analytical solution.

where $A(i)$ is defined as:

$$A(i) = \frac{n_i}{1+n_i}\left(-\frac{\partial P}{\partial x}.\frac{1}{K_i}\right)^{(1/n_i)} \tag{36}$$

In our simulations, the domain has a length of L=5H, and h=H/2 while a mesh with grid size of H/80 is used to discretize the domain. A constant pressure gradient of $\frac{\partial P}{\partial x} = 0.075$ and a surface tension coefficient of 24.5 $[J/m^2]$ is being applied in all the cases. Simulations with different rheological properties have been performed for a long enough time. The details of rheological properties of these cases are tabulated in table 4. For each case, the first norm of error of numerical simulation is calculates using: $L_1 = \sum_i |e_i|$, where e_i is the point-wise error of each cell compared with its analytical solution. The value of L_1 for all of these cases are presented in table 4. As can be seen in this table, the value of the L_1 for all the cases is in the order of $\approx O(10^{-3})$, which is considered as good agreement.

4.2. Impacting droplet problem

In this section, using the numerical method proposed, the falling of a two-dimensional viscoelastic droplet under gravitational force with the acceleration of g is being solved. The droplet with an initial diameter of d_0 is placed at the height of $H = 2d_0$ above a stationary plate. The computational domain has a length of

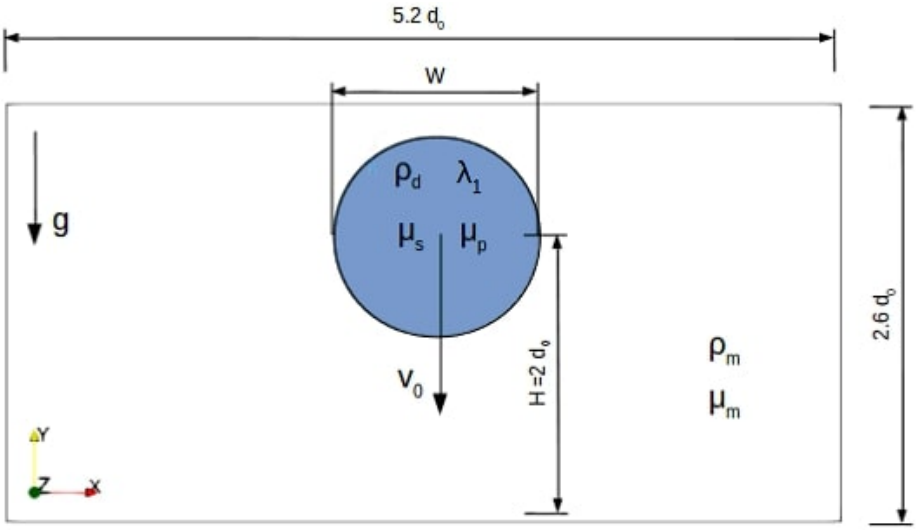

Figure 4: Initial computational setup of the impacting droplet problem.

$5.6d_0$ and a height of $2.6d_0$. Two different grid types of structured and unstructured are used to discretize the solution domain. Figure 4 illustrates the initial setup of the problem. At time $t/t^* = 0.0$, the droplet falls towards the wall with an initial velocity of V_0 (with $t^* = d_0/V_0$). Oldroyd-B constitutive equation is used to model the viscoelastic behaviour of the droplet with a retardation ratio of $\beta = 0.1$, while the effect of surface tension is neglected. Three sets of non-dimensional parameters of Reynolds (Re), Deborah (De) and Froude (Fr) numbers are used as below:

$$Re = \frac{\rho_d d_0 V_0}{\mu_{0d}} = 5 \quad De = \frac{\lambda_1 V_0}{d_0} = 1 \quad Fr = \frac{V_0}{\sqrt{g d_0}} = 2.26 \tag{37}$$

No-slip boundary condition is applied on the bottom wall while the free-slip boundary condition is applied on all the other walls. In this work, no contact line model is used. More details on the physics of the impacting droplet problem, and the related contact line models could be found in [85, 86, 87]. In order to minimize the effect of the matrix gas, a density and viscosity ratio of $\rho_d/\rho_m = \mu_{0d}\mu_m = 1000$ is used. Figure 5 shows the time evolution of the non-dimensional width of the droplet (W/d_0) for the solution done in this study in domains with structured and unstructured grids in comparison with results of different approaches available in literature, e.g. (SPH) method of Fang et al. [19], Jiang et al. [20] and MAC method of Oishi

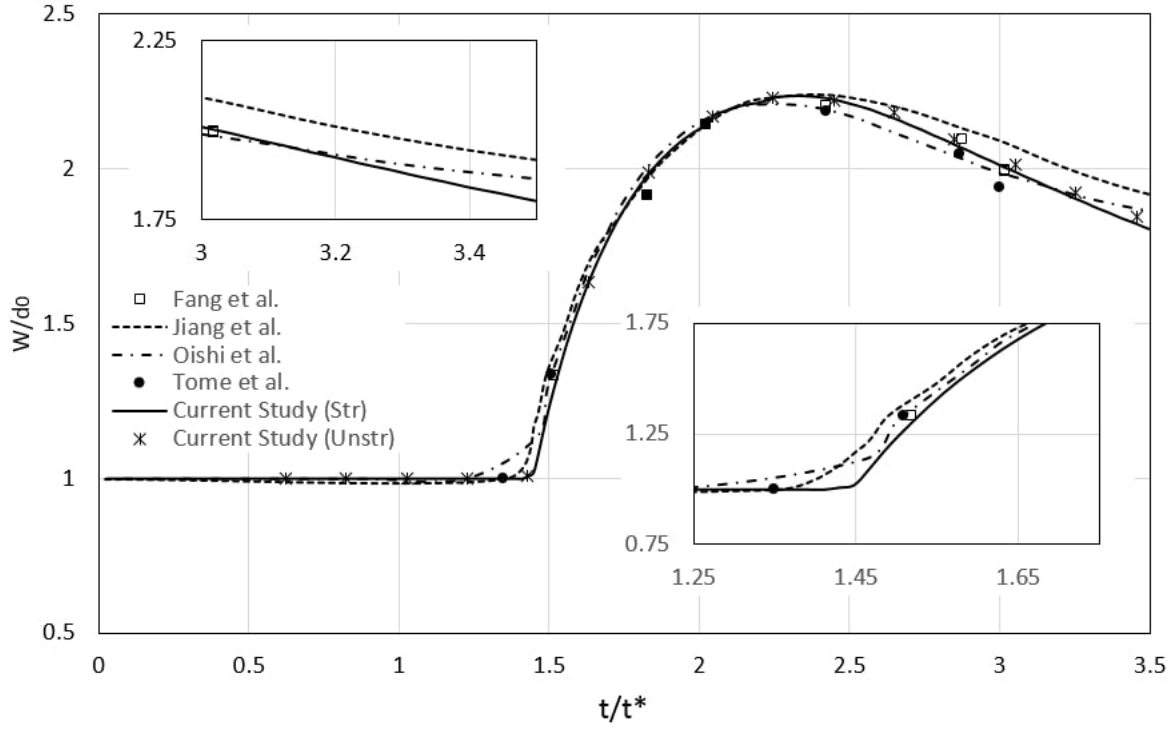

Figure 5: Time evolution of non-dimensional width of an Oldroyd-B droplet impacting on a surface for simulations with two different grid types of structured (Str) and unstructured (Unstr). The results of current study are compared with the (SPH) results of Fang et al. [19], Jiang et al. [20] and MAC results of Oishi et al. [10], Tomé et al. [9]

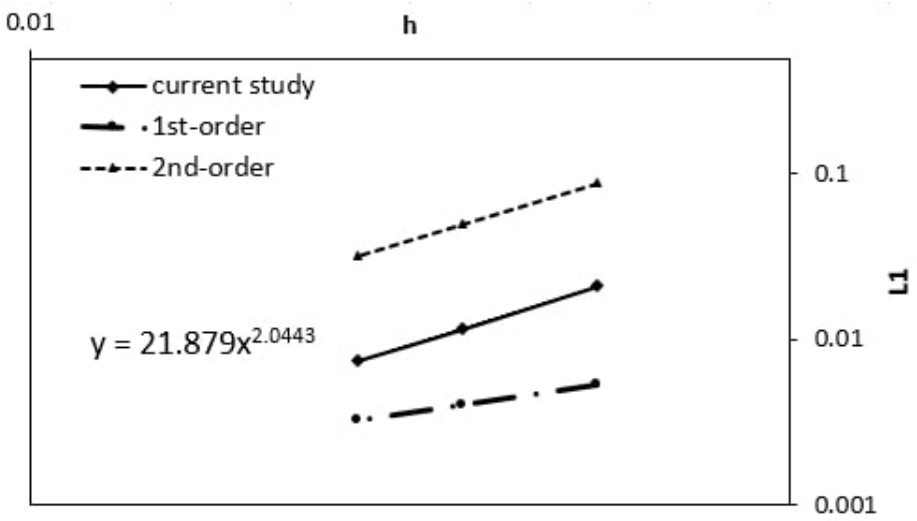

Figure 6: First norm of the error in calculation of width of the droplet (W) during the solution process of the impacting droplet problem inside of the domains with structured grids with sizes of $h = d_0/30, d_0/40$ and $d_0/50$ compared with the reference values of solution in a domain with the grid size of $h = d/60$.

et al. [10], Tomé et al. [9]. Good agreement is seen for simulations both in structured and unstructured grids in comparison to the aforementioned results available in the literature.

A grid convergence study is performed for this case. Simulations of the reported case in a domain with structured grids with four different grid sizes of $h = d_0/30, d_0/40, d_0/50$ and $h = d_0/60$ are done. For each case, the numerical simulation performed until $t/t^* = 3.5$. The variation of the width of the droplet (W) for the solution with the finest grid ($h = d_0/60$) is selected as the reference, where the results of other simulations are compared with it, to calculate the error associated to the droplet width (W) at each timestep. The accumulated value of these errors are measured as the first norm of the error using $L_1 = \sum_i |e_i|$, where e_i is the difference between droplet width (W) of the simulation and its corresponding value in reference solution at i-th iteration. Figure 6 presents the values of L_1 as a function of the grid size. As can be seen, the solution process illustrates an order of convergence of 2.04 in space.

Trace of the conformation tensor indicates the elongation of the polymer chains (EPC). Figure 7 illustrates the snapshots of the droplet evolution, with the contours of elongation of the polymer chains. As can be seen, upon the impact of the droplet, the length of the polymeric chains increases in the triple points of

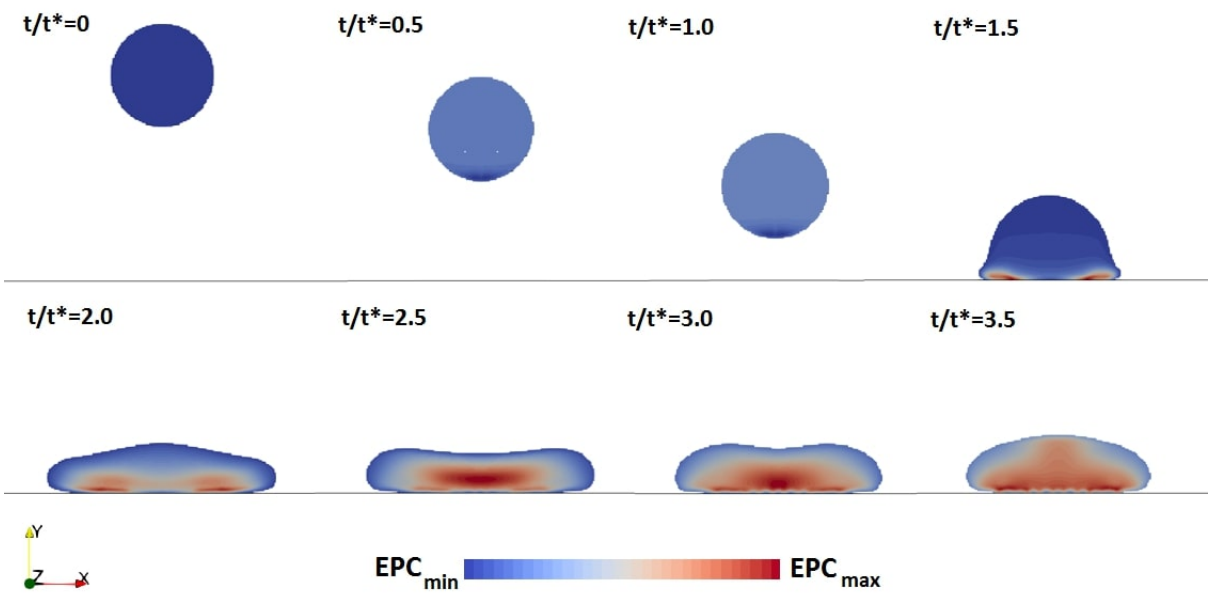

Figure 7: Snapshots of the impact of a viscoelastic droplet over a surface. The color contours present the elongation of the polymer chains (EPC) in the droplet.

the contact and spreads in spatial areas around this region. As the droplet evolves toward equilibrium, the length of the polymeric chains expands in the droplet core.

4.3. Sudden contraction/expansion

In this section, numerical simulation of a viscoelastic droplet suspended in Newtonian matrix, passing through a contraction/expansion geometry is done and the results are compared against available experimental images. Figure 8 illustrates the schematic representation of the domain's dimensions and mesh configuration. All the lengths are non-dimensionalized by the inlet's half width, H_{in}. Two types of meshes of structured cubic cells and unstructured triangular-prism cells with the edge size of $h = H_{in}/36$ are used to discretize the domain. To approximate the experimental dimensions, the contraction and expansion edges are bevelled with a side length of $0.1H_{in}$. The width of the domain in Z direction is $W = 0.33H_{in}$. A flow with uniform velocity of (U,V,W)=($\overline{U}$,0,0) enters the domain through the inlet and exits the domain through the outlet boundary conditions. Non-wetting boundary condition for level-set function, no-slip boundary condition for velocity components and Neumann boundary condition for pressure and extra-stress

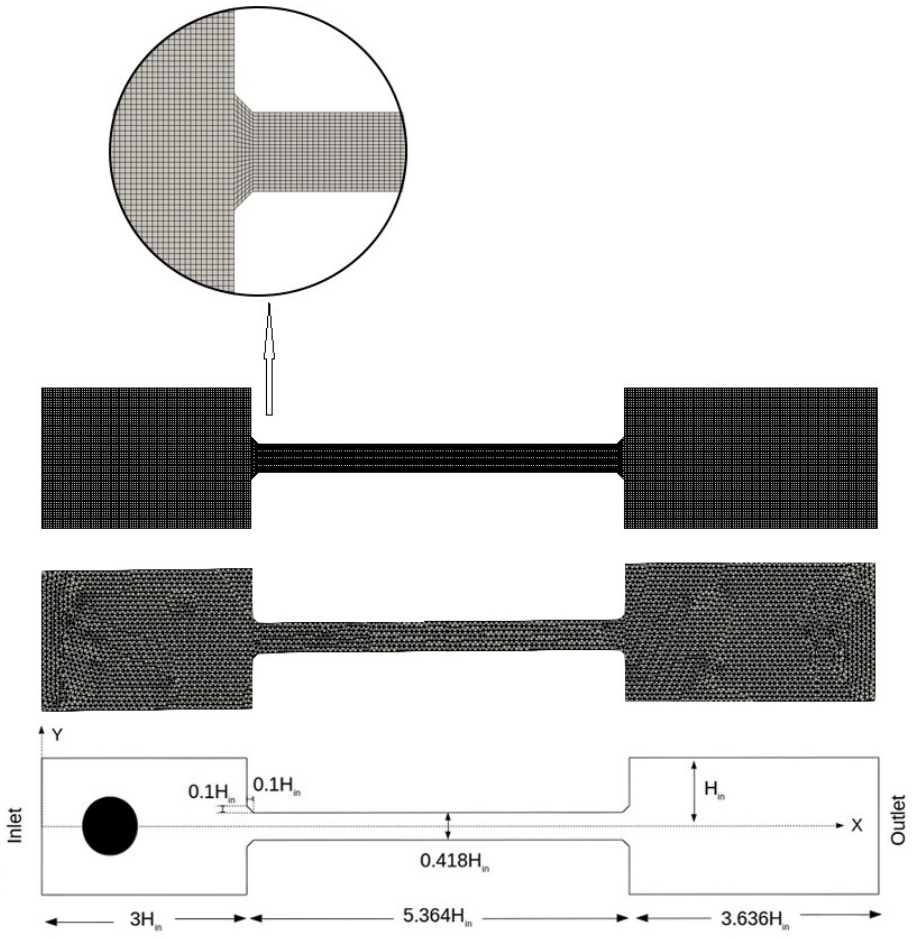

Figure 8: schematic representation of domain's dimensions and mesh configuration of sudden contraction/expansion test case with two different mesh types of structured and unstructured grids.

tensor are applied on the walls. A droplet with initial diameter of $d_0 = 0.864H_{in}$ is places in a quiescent Newtonian matrix. The Oldroyd-B constitutive equation is used to model the viscoelastic behavior of the droplet. Non-dimensional group of variables as below are used in addition to density ratio (ρ_d/ρ_m), total viscosity ratio (μ_{0d}/μ_{0m}) and retardation ratio (β) to physically define the problem:

$$Re = \frac{\rho_m \overline{U} H_{in}}{\mu_m} \quad We = \frac{\rho_m \overline{U}^2 H_{in}}{\sigma} \quad De = \frac{\lambda_1 \overline{U}}{H_{in}} \tag{38}$$

Time is non-dimensionalized as t/t^* with $t^* = (H_{in}/\overline{U})$. Table 5, presents the selected characteristics of the problem based on the introduced non-dimensional group of variables. The droplet is being imposed to

Table 5: Non-dimensional parameters defining the sudden contraction/expansion test case

Re	We	De	ρ_d/ρ_m	μ_{0d}/μ_{0m}	β
0.825	6.22×10^{-2}	0.598	1.17	31	0.586

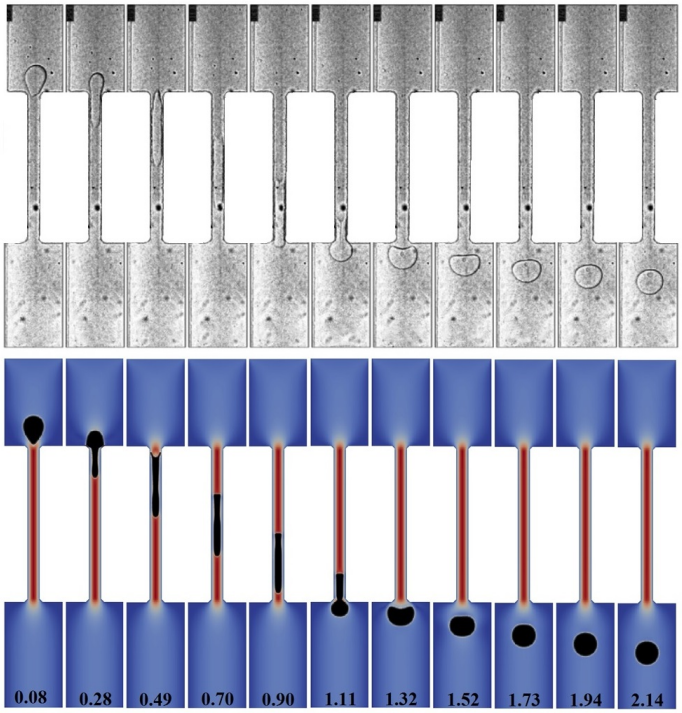

Figure 9: Sudden contraction/expansion of a viscoelastic droplet in a Newtonian matrix. Top: experiment results of [88], Bottom: results of current study, extracted at the same time instances of experimental images.

a geometrical contraction, is forced to change its shape in order to pass through the narrow channel, and retrieves its more stable spherical shape after passing through the expansion. The simulation continues until $t/t^* = 2.14$. Figure 9 presents the results of the numerical simulation of the current study in structured grid compared with the experimental results of [88] for the same time instances. Please note, since the results obtained by structured grid were identical to the results of unstructured grid, in order to avoid redundancy, only the results obtained with one of them is being shown. In this figure, non-dimensional times of the simulations are provided at the bottom of the image. Note that the reference time of $t/t^* = 0.0$ is when the leading tip of the droplet enters the contraction zone. According to this figure, very good agreement is seen between the results of current study, and experimental results of Harvie et al. [88], which validates the

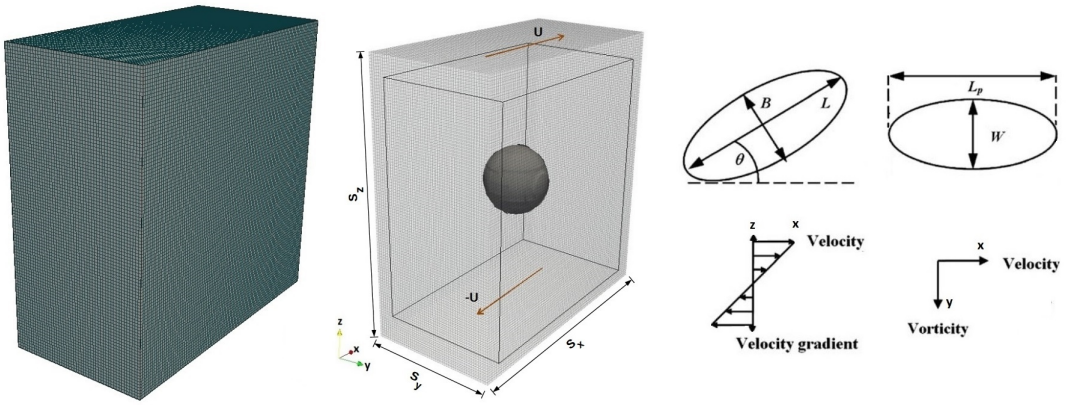

Figure 10: Left: Mesh configuration, structured cubic cells. Middle: computational setup, Right: Schematic presentation of a deformed droplet along with related geometrical measurements in velocity-velocity gradient, and velocity-vorticity planes.

ability of the proposed method on capturing the physics of this problem.

4.4. Simple Shear flow

A circular Newtonian droplet with diameter d is suspended in a viscoelastic matrix in a domain with span $S_x = 5d$, $S_y = 5d$ and $S_z = 2.5d$ in x,y and z directions, respectively. Figure 10 illustrates the mesh configuration and computational setup. The opposite x-direction velocities of $+U$ and $-U$ are imposed at the top and bottom walls inducing a shear rate of $\dot{\gamma} = 2U/S_z$ in the domain. A periodic boundary condition is applied in the flow direction (x) and Neumann boundary condition in y direction. Computations have been performed using a Cartesian mesh of cubic cells with the edge size of h=d/30. This mesh was generated by a constant step extrusion of the two-dimensional y-z grid along the x-axis with the step size of h. A grid convergence analysis is provided at the end of this section for the most challenging cases. At the beginning of the simulation, a linear velocity field is applied inside of the domain varying from $-U$ at the bottom wall to $+U$ at the top wall.

For Newtonian droplet and matrix, the system can be physically defined by four parameters of Reynolds number (Re), Capillary number (Ca), total viscosity ratio (μ_{0d}/μ_{0m}) and walls confinement ratio ($2r/S_z$). For an arbitrary value of shear rate ($\dot{\gamma}$), the velocity at the top and bottom walls are calculated as $U = \dot{\gamma}S_z/2$.

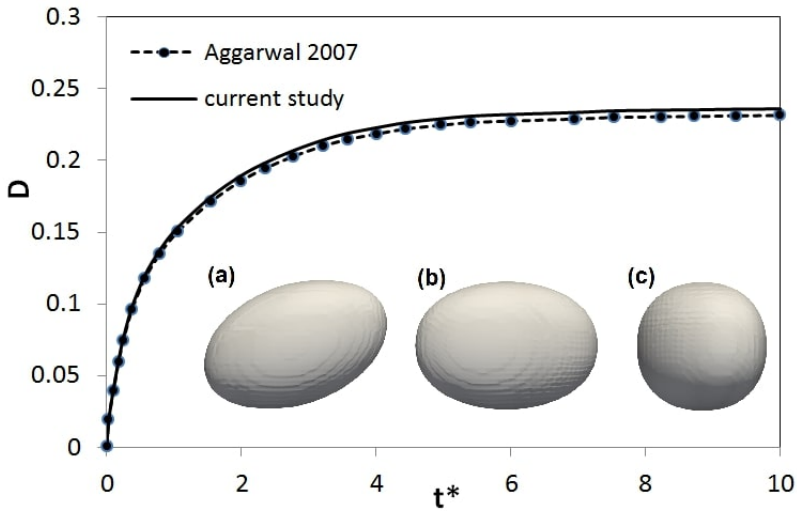

Figure 11: Taylor deformation parameter (D) vs. time ($t' = t\dot{\gamma}$) for a Newtonian droplet suspended in viscoelastic matrix imposed to a shear with Re=0.1, Ca=0.2 and De=1.5 compared with results of Aggarwal and Sarkar [16]. Sub-figures of (a), (b) and (c) present the droplet shape at $t' = 10$ in (X-Y), (X-Z) and (Y-X) planes, respectively.

Then viscosity is calculated using the Reynolds number as below:

$$Re = \frac{\rho_m \dot{\gamma} r^2}{\mu_{0m}} \tag{39}$$

where r is the droplet's radius. The Capillary number is a dimensionless parameter defining the relative effect of the shear stress versus surface tension across the interface, given by:

$$Ca = \frac{\dot{\gamma} \mu_{0m} r}{\sigma} \tag{40}$$

For a given value of Ca and Re numbers, and the calculated value of μ_{0m}, the related value of σ is determined.

In the case where the droplet evolves to a steady shape, different parameters have been used to measure the deformation attained by the droplet. The first one is the Taylor deformation parameter defined as $D = (L - B)/(L + B)$, where L and B are length and breadth of the drop, as shown in figure 10. Another parameter is the angle θ of orientation of the droplet with respect to the axis of shear strain. In addition

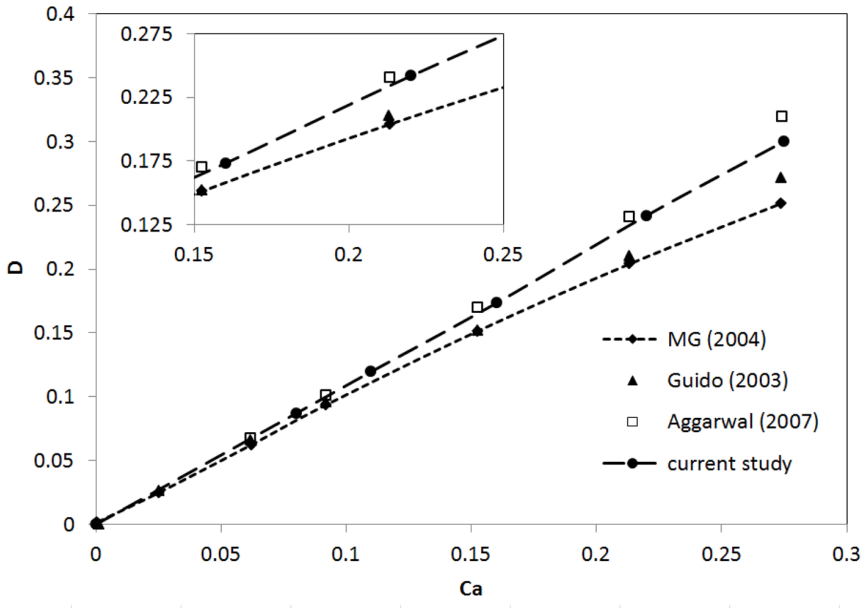

Figure 12: Steady-state Taylor deformation parameter (D) for simulations of a Newtonian droplet in viscoelastic matrix with different values of Capillary numbers, all with elasticity parameter of p=De/Ca=0.6. Results of current study are compared with the results of three different approaches, experimental data of Guido et al. [89], analytical predictions of Maffettone and Greco [90] and numerical results of Aggarwal and Sarkar [16].

to these parameters, L_p and W, as projected length and width of the droplet are used in literature and depicted in figure 10.

For viscoelastic rheological characteristics of the matrix, Oldroyd-B constitutive equation is solved. The initial condition of conformation tensor is Identity tensor in the whole domain leading to zero stress initial condition. Non-dimensional parameter of Deborah number ($De = \lambda_1 \dot{\gamma}$) and retardation ratio are used in addition to the four previously defined parameters of Re, Ca, total viscosity ratio and walls confinement ratio to fully define the system. In all the simulations, a low Reynolds number of 0.1, retardation ratio of $\beta = 0.5$, and droplet to matrix total viscosity ratio of 1 is being applied.

The accuracy of the proposed method on capturing the transient solution of this problem is studied by performing a simulation with Capillary number of 0.2 and Deborah number of 1.5. Figure 11 shows the time variation of Taylor deformation parameter (D) for this case compared with the results of finite-

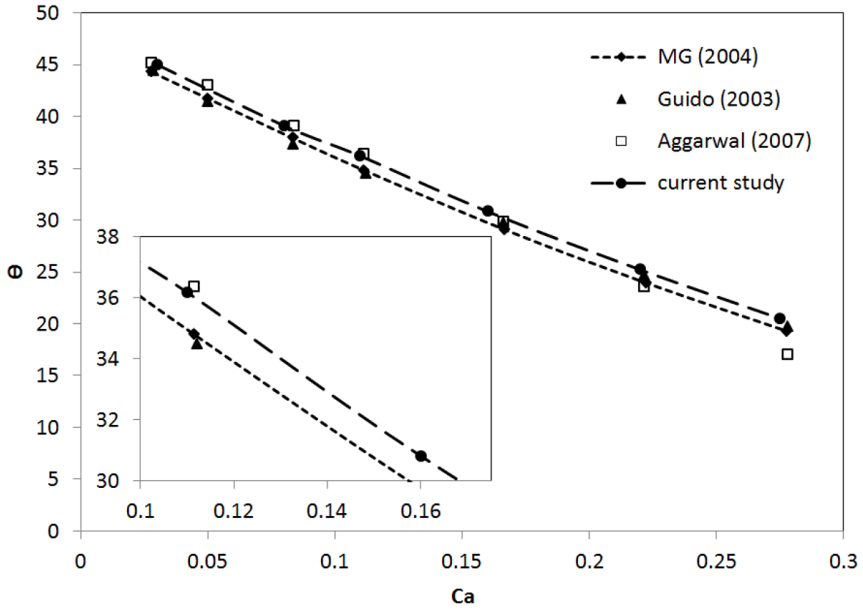

Figure 13: Droplet inclination angel (θ) parameter for simulations of a Newtonian droplet in viscoelastic matrix with different values of Capillary numbers, all with elasticity parameter of p=De/Ca=0.6. Results of current study are compared with the results of three different approaches, experimental data of Guido et al. [89], analytical predictions of Maffettone and Greco [90] and numerical results of Aggarwal and Sarkar [16].

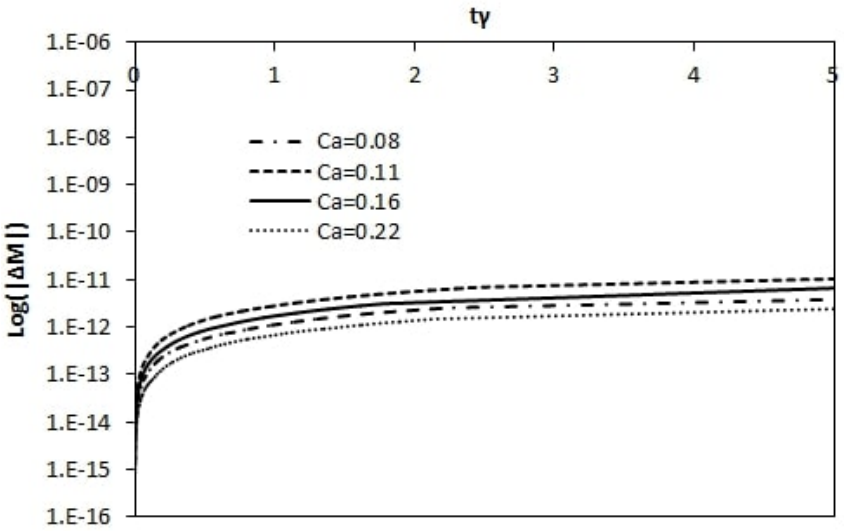

Figure 14: The evolution in the mass conservation error of the droplet for cases of Newtonian droplet suspended in viscoelastic matrix imposed to shear with four different Capillary numbers of 0.08, 0.11, 0.16 and 0.22, and Deborah numbers of $De = 0.6 \times Ca$. The value of ΔM for the droplet is $(M_t - M_0)/M_0$, where M_0 is droplet's initial mass and M_t is the mass at time t.

difference/front-tracking method of Aggarwal and Sarkar [16]. Good agreement is seen between these results.

In order to study the accuracy of the method on solving this problem for a wider range of Deborah numbers, simulations with different Capillary numbers but all with a constant elasticity parameter of P=De/Ca=0.6 are done for a long enough time to reach steady-state. For each case, Taylor deformation parameter (D), and droplet inclination angel of θ are extracted. Figures 12 and 13 illustrates these results compared with results of different methods, i.e. experimental data of Guido et al. [89], analytical predictions of Maffettone and Greco [90] and numerical results of Aggarwal and Sarkar [16]. Good agreement is seen between the results of current study, and the results of numerical study of Aggarwal and Sarkar [16] in all the cases. There is also a good agreement between the results of current study, and the experimental data of Guido et al. [89] and also analytical predictions of Maffettone and Greco [90] for smaller Capillary numbers. For higher Capillary numbers in these two figures, however, the disparity of the numerical results compared with experimental data and analytical predictions grows. This disparity could be associated to the inability of the Oldroyd-B constitutive equation used in this study to correctly represents the experimental fluid used

by Guido et al. [89]. Figure 14 represents the evolution of mass conservation error of the droplet for different cases solved in this section. It could be seen that for all these cases, the mass conservation error of the droplet, ΔM, (calculated as $\Delta M = (M_t - M_0)/M_0$, with M_0 as droplet's initial mass and M_t as the mass at time t) has converged to a very small value in the order of $O(10^{-11})$.

In order to study the ability of the method in solving more challenging cases, the LCR method, integrated with cut-off approach is used to solve three high Deborah number shear deformation problems of:

(a) Newtonian droplet suspended in viscoelastic matrix with Deborah number of 5.0.

(b) Viscoelastic droplet with Deborah number of 7.5 suspended in a Newtonian matrix.

(c) Viscoelastic droplet with Deborah number of 7.5 suspended in a viscoelastic matrix with Deborah number of 5.0.

In all these cases, the $Re = 1.0$, $Ca = 2.0$, $\beta = 0.5$ and $\mu_{d0}/\mu_{m0} = 1.0$ are applied. Simulation of case (b) was converged to steady-state within the limit of $t/t^* = 10$. Cases (a) and (c), however, required more time to reach steady-state. Figure 15 presents the Taylor deformation (D), L_P and W parameters as introduced in figure 10, as a function of time. There is an overshoot in the value of Taylor deformation parameter of case (b).The overshoots in sub-critical deformation of Newtonian droplets suspended in Newtonian matrix happens only in highly confined domains. Thus the overshoot in the value of D witnessed in figure 15, corresponds to the non-Newtonian highly viscoelastic nature of the droplet.

Case (a) on the other hand, exhibits a more uniform deformation, carried on with a retraction in deformation of the droplet at times around $t/t^* = 14$. Similar to case (b), in case (c), at times around $t/t^* = 1$ there is an overshoot in deformation of the droplet. By observing the existence of overshoot in deformation of the droplets, in cases (b) and (c) and its absence in case (a), one can conclude that the highly viscoelastic nature of the droplet can cause the droplet to retract after an initially larger deformation, and undertake overshoots in its deformation. On the other hand, by observing a more uniform deformation of the droplet in cases (a) and (c), one can conclude that the viscoelastic nature of the matrix results in a more smooth deformation of the droplet over time.

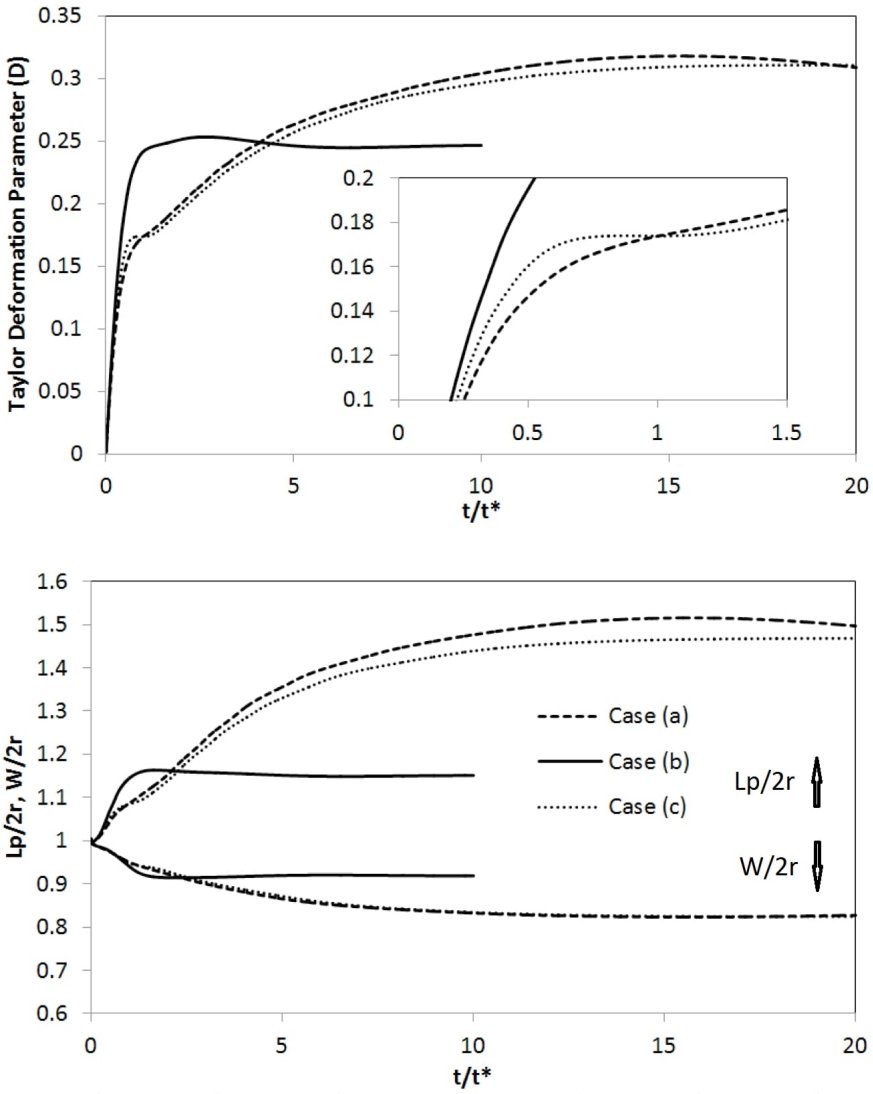

Figure 15: Startup variation of Top: Taylor Deformation Parameter (D) and Bottom: $L_p/2r$ and W/2r parameters Vs. t/t^* for cases (a), (b) and (c) of droplet deformation in shear flow.

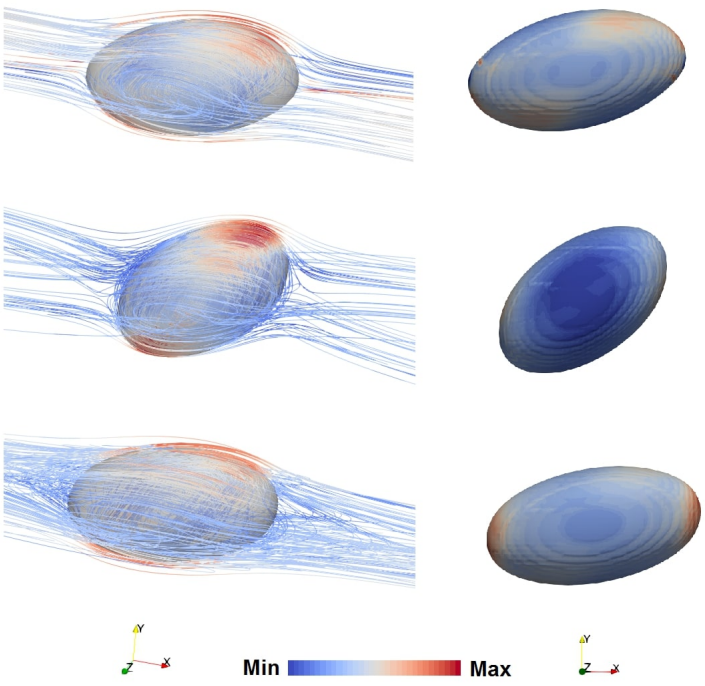

Figure 16: Left: droplets shape along with the flow streamlines with vorticity magnitude contours, Right: droplets shape along with pressure contours. Images correspond to the cases, Top: case (a) extracted at t/t^*=20, Middle: case (b) extracted at t/t^*=10, and Bottom: case (c) extracted at t/t^*=20.

Figure 16 illustrates the droplets shape along with the flow streamlines with vorticity magnitude and pressure contours for the cases (a), (b) and (c) at the end of the solution process. According to this figure, The viscoelastic matrix causes that the Newtonian droplet to loose its elliptical shape. Droplet inclination angel of case (b) is notably higher than the other two cases, which is in agreement with its lower Taylor deformation parameter. In the solution process of all of these cases, no numerical difficulties were witnessed.

A grid convergence analysis is performed for the case (c), viscoelastic droplet with Deborah number of 7.5 suspended in a viscoelastic matrix with Deborah number of 5.0. Four different grid sizes of h=d/25, d/30, d/35 and d/40 are selected to discretize the aforementioned domain. For each case, the numerical simulation was done until $t/t^* = 20$. The variation of Taylor deformation parameter (D) of the solution with the finest grid (h=d/40) is selected as the reference data and the results of other simulations are compared with it. For each case, the error related to the Taylor deformation parameter (D) at each timestep is calculated.

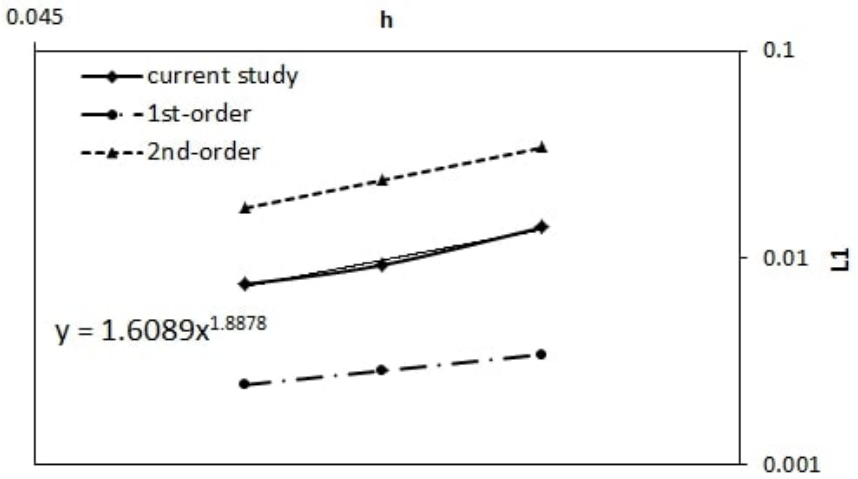

Figure 17: First norm of the error in calculation of Taylor deformation parameter (D) during the solution process of the case (c) inside of the domains with grid sizes of $h = d/25, d/30$ and $d/35$ compared with the reference values of solution in a domain with grid size of $h = d/40$.

Accumulated value of these errors are calculated as the first norm of the error using $L_1 = \sum_i |e_i|$, where e_i is the difference between Taylor deformation parameter of the simulation and its corresponding value in reference solution at i-th iteration. Figure 17 presents the values of L_1 as a function of the grid size. As can be seen, the solution process illustrates an order of convergence of 1.88 in space.

We perform a series of numerical simulations to examine the parallel scalability of our numerical approaches and computer code by solving the test case (c) of this section, i.e. viscoelastic droplet with Deborah number of 7.5 suspended in a viscoelastic matrix with Deborah number of 5.0. The discretized domain is the same as before, but with a more fine grid size of $h = r/35$, leading to a total number of 21.4×10^6 grid cells. These test cases were solved on the supercomputer MareNostrum IV based in Barcelona, Spain by using 528, 1056, 2112, 3160 and 4224 processors. The computer time in the solution of one-iteration of the global algorithm for all these cases is extracted, and time in solution with 528 processors is used as a reference value (T_{ref}). Figure 18 (left) presents the normalized computer time (T_{comp}/T_{ref}) for solution with different number of processors, and figure 18 (right) presents the strong speed-up (SSU) (T_{ref}/T_{comp}) graph.

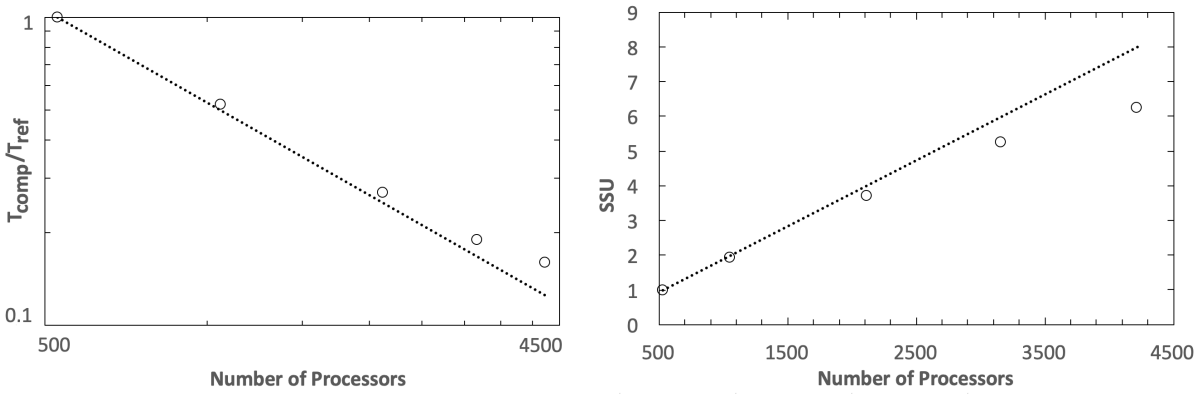

Figure 18: Parallel scalability of the numerical methodology and computer code of current paper. Left: normalized computing time (T_{comp}/T_{ref}) of one-iteration of global algorithm described in section 3.6, right: strong speed-up, linear (dash-line) and current study (circular-symbols).

5. Conclusion

A finite-volume conservative level-set based method was introduced in order to solve non-Newtonian multiphase flow problems. The main challenges in this area including tracking of interfaces, mass conservation of the phases, small timestep problems encountered by non-Newtonian fluids, numerical instabilities regarding the high Weissenberg number problem (HWNP), instabilities encouraged by low solvent to polymer viscosity ratio in viscoelastic fluids (LVRP) and instabilities encountered by surface tensions were addressed and proper numerical treatments were provided in the proposed method. For small timestep problem, specially in shear-thinning and shear-thickening fluids where the unexpected increase in kinematic viscosity can dramatically decrease the timestep of the simulation, our proposed discretization method successfully eliminated the timestep restrictions encountered by viscosity. The proposed cut-off approach was investigated for different viscoelastic combinations of droplet/matrix. Using this approach enables us to substitute the SAM method with LCR formulation, resulting in elimination of HWNP for multiphase fluids. The proposed discretization of predictor step of momentum equation eliminated the LVRP for a challenging case with $\beta = 0.0014$. The conservative formulation of the level-set function preserves the mass of the droplet during the whole simulation.

Different test cases with different rheological properties were solved in order to validate the accuracy of

the method. The fluid of a Poiseuille flow was solved for rheologies of shear-thinning, shear-thickening and viscoelastic fluids and the results were compared with analytical exact solutions. For viscoelastic droplet, a test case of impacting droplet problem was selected and the results were compared with the available data in literature. A three-dimensional sudden contraction/expansion test case was solved and the results were compared with the experimental figures. For viscoelastic matrix, a three-dimensional shear deformation problem was solved for a wide range of Deborah parameters. The extracted results were compared with analytical, experimental and numerical predictions. In all these cases, good agreement was seen between the results extracted in the current study, and the benchmark data available in the literature. In addition to validation cases, three challenging high Wissembourg number test cases were solved and the results were discussed.

Acknowledgments

This work has been financially supported by the *Ministerio de Economía y Competitividad, Secretaría de Estado de Investigación, Desarrollo e Innovación*, Spain (ENE2015-70672-P). The authors thankfully acknowledge the computer resources at Altamira and the technical support provided by Instituto de Física de Cantabria - Universidad de Cantabria (RES-FI-2018-3-0045). A. Amani acknowledges the financial support of an FI research scholarship by the *Agència de Gestió d'Ajuts Universitaris i de Recerca (AGAUR) of Generalitat de Catalunya* (2016 FI_B 01059). N. Balcázar acknowledges the financial support of the Programa Torres Quevedo (PTQ-14-07186).

Appendix A. Derivation of formulation of Log-conformation representation method

We can consider the formulation for the eigendecomposition of the positive-definite tensor of $\mathbf{c}$ in three-dimensional space as $\mathbf{c} = \mathbf{R}\,\mathbf{\Lambda}\,\mathbf{R}^T$ with $\mathbf{R}$ as the orthogonal matrix containing the eigenvectors of $\mathbf{c}$ and $\mathbf{\Lambda}$ as a diagonal matrix containing the corresponding eigenvalues. By substituting the $\mathbf{c} = \mathbf{R}\,\mathbf{\Lambda}\,\mathbf{R}^T$ in equation

8 and defining $L := \nabla \mathbf{v}$, we will have:

$$\frac{D\boldsymbol{R}}{Dt}\boldsymbol{\Lambda}\boldsymbol{R}^T + \boldsymbol{R}\frac{D\boldsymbol{\Lambda}}{Dt}\boldsymbol{R}^T + \boldsymbol{R}\boldsymbol{\Lambda}\frac{D\boldsymbol{R}^T}{Dt} = \boldsymbol{R}\boldsymbol{\Lambda}\boldsymbol{R}^T\boldsymbol{L} + \boldsymbol{L}^T\boldsymbol{R}\boldsymbol{\Lambda}\boldsymbol{R}^T - \frac{1}{\lambda_1}f_r(\boldsymbol{R}\boldsymbol{\Lambda}\boldsymbol{R}^T) \tag{A.1}$$

Multiplying $\boldsymbol{R}^T$ and $\boldsymbol{R}$ into this equation from left and right, respectively, will result in:

$$\boldsymbol{R}^T\left[\frac{D\boldsymbol{R}}{Dt}\boldsymbol{\Lambda}\boldsymbol{R}^T + \boldsymbol{R}\frac{D\boldsymbol{\Lambda}}{Dt}\boldsymbol{R}^T + \boldsymbol{R}\boldsymbol{\Lambda}\frac{D\boldsymbol{R}^T}{Dt}\right]\boldsymbol{R} = \boldsymbol{R}^T\left[\boldsymbol{R}\boldsymbol{\Lambda}\boldsymbol{R}^T\boldsymbol{L} + \boldsymbol{L}^T\boldsymbol{R}\boldsymbol{\Lambda}\boldsymbol{R}^T - \frac{1}{\lambda_1}f_r(\boldsymbol{R}\boldsymbol{\Lambda}\boldsymbol{R}^T)\right]\boldsymbol{R} \tag{A.2}$$

Defining the skew-symmetric matrix of $\tilde{\Omega} := \boldsymbol{R}^T\frac{D\boldsymbol{R}}{Dt}$ and matrix of $\tilde{L} := \boldsymbol{R}^T L\boldsymbol{R}$ and substituting them in A.2, will result in:

$$\tilde{\boldsymbol{\Omega}}\boldsymbol{\Lambda} + \boldsymbol{\Lambda}\tilde{\boldsymbol{\Omega}}^T + \frac{D\boldsymbol{\Lambda}}{Dt} = \boldsymbol{\Lambda}\tilde{\boldsymbol{L}} + \tilde{\boldsymbol{L}}^T\boldsymbol{\Lambda} - \frac{1}{\lambda_1}\boldsymbol{R}^T f_r(\boldsymbol{R}\boldsymbol{\Lambda}\boldsymbol{R}^T)\boldsymbol{R} \tag{A.3}$$

In this equation, the first two terms in the left hand side ($\tilde{\boldsymbol{\Omega}}\boldsymbol{\Lambda} + \boldsymbol{\Lambda}\tilde{\boldsymbol{\Omega}}^T$) are skew-symmetric and while $\frac{D\boldsymbol{\Lambda}}{Dt}$ is a diagonal matrix. As a result, the off-diagonal elements of the resultant matrix of right hand side of equation A.3 will be equal to $\tilde{\boldsymbol{\Omega}}\boldsymbol{\Lambda} + \boldsymbol{\Lambda}\tilde{\boldsymbol{\Omega}}^T$ and diagonal elements of it will be equal to $\frac{D\boldsymbol{\Lambda}}{Dt}$. From this notion, the values of $\tilde{\boldsymbol{\Omega}}$ and $\frac{D\boldsymbol{\Lambda}}{Dt}$ will be obtained as:

$$\left(\frac{D\boldsymbol{\Lambda}}{Dt}\right)_{ii} = 2\Lambda_{ii}\tilde{L}_{ii} - \frac{1}{\lambda_1}\left(\boldsymbol{R}^T f_r(\boldsymbol{R}\boldsymbol{\Lambda}\boldsymbol{R}^T)\boldsymbol{R}\right)_{ii}, \quad \text{for i } \in \{1,2,3\} \tag{A.4}$$

$$\tilde{\Omega}_{ij} = \frac{\Lambda_{ii}\tilde{L}_{ij} + \tilde{L}_{ji}\Lambda_{jj} - \frac{1}{\lambda_1}\left(\boldsymbol{R}^T f_r(\boldsymbol{R}\boldsymbol{\Lambda}\boldsymbol{R}^T)\boldsymbol{R}\right)_{ij}}{\Lambda_{jj} - \Lambda_{ii}}, \qquad \text{for i} \neq \text{j} \tag{A.5}$$

As mentioned before, the log-conformation representation method uses a change of variable in the constitutive model in term of the matrix-logarithm of the conformation tensor as below:

$$\boldsymbol{\Psi} = \text{Ln } \mathbf{c} = \boldsymbol{R}\,\text{Ln}\boldsymbol{\Lambda}\,\boldsymbol{R}^T \tag{A.6}$$

Keeping in mind the definition of $\tilde{\Omega} := \boldsymbol{R}^T \frac{D\boldsymbol{R}}{Dt}$, and applying the material derivative operator to left and right hand sides of above equation, we will have:

$$\frac{D\boldsymbol{\Psi}}{Dt} = \boldsymbol{R}\left[\left(\tilde{\boldsymbol{\Omega}}\,\mathrm{Ln}\boldsymbol{\Lambda} + \mathrm{Ln}\boldsymbol{\Lambda}\,\tilde{\boldsymbol{\Omega}}^T\right) + \frac{D\boldsymbol{\Lambda}}{Dt}\boldsymbol{\Lambda}^{-1}\right]\boldsymbol{R}^T \tag{A.7}$$

Since $\frac{D\boldsymbol{\Lambda}}{Dt}\boldsymbol{\Lambda}^{-1}$ is a diagonal matrix, and $(\tilde{\boldsymbol{\Omega}}\,\mathrm{Ln}\boldsymbol{\Lambda} + \mathrm{Ln}\boldsymbol{\Lambda}\,\tilde{\boldsymbol{\Omega}}^T)$ is a skew-symmetric matrix, with the help of equations A.4 and A.5, their values could be extracted as:

$$\left(\frac{D\boldsymbol{\Lambda}}{Dt}\boldsymbol{\Lambda}^{-1}\right)_{ii} = 2\tilde{L}_{ii} - \frac{1}{\lambda_1\Lambda_{ii}}\left(\boldsymbol{R}^T f_r(\boldsymbol{R}\boldsymbol{\Lambda}\boldsymbol{R}^T)\boldsymbol{R}\right)_{ii}, \text{for i } \in \{1,2,3\} \tag{A.8}$$

$$\begin{aligned}\left(\tilde{\boldsymbol{\Omega}}\,\mathrm{Ln}\boldsymbol{\Lambda} + \mathrm{Ln}\boldsymbol{\Lambda}\,\tilde{\boldsymbol{\Omega}}^T\right)_{ij} &= \\ \tilde{\Omega}_{ij}\left(\mathrm{Ln}\Lambda_{jj} - \mathrm{Ln}\Lambda_{ii}\right) &= \\ \left[\frac{\Lambda_{ii}\tilde{L}_{ij} + \tilde{L}_{ji}\Lambda_{jj} - \frac{1}{\lambda_1}\left(\boldsymbol{R}^T f_r(\boldsymbol{R}\boldsymbol{\Lambda}\boldsymbol{R}^T)\boldsymbol{R}\right)_{ij}}{\Lambda_{jj} - \Lambda_{ii}}\right]&\left(\mathrm{Ln}\Lambda_{jj} - \mathrm{Ln}\Lambda_{ii}\right), \text{for i} \neq \text{j}\end{aligned} \tag{A.9}$$

For the sake of clarity, we define some extra variables as below:

$$\tilde{\boldsymbol{G}} = \boldsymbol{R}^T f_r(\boldsymbol{R}\boldsymbol{\Lambda}\boldsymbol{R}^T)\boldsymbol{R} \qquad \boldsymbol{G} = \boldsymbol{R}\,\tilde{\boldsymbol{G}}\,\boldsymbol{R}^T$$

$$\tilde{\boldsymbol{L}} = \boldsymbol{R}^T\,\boldsymbol{L}\,\boldsymbol{R} \qquad \boldsymbol{L} = \nabla\mathbf{v}$$

$$\tilde{\boldsymbol{B}} = \text{Diagonal matrix of}(\tilde{\boldsymbol{L}}) \qquad \boldsymbol{B} = \boldsymbol{R}\tilde{\boldsymbol{B}}\boldsymbol{R}^T$$

Using these variables, and definitions of equations A.8 and A.8, and taking into account that $\Lambda^{-1} = \boldsymbol{R}^T e^{-\Psi}\,\boldsymbol{R}$, the equation A.7 could be written as:

$$\frac{D\boldsymbol{\Psi}}{Dt} = \boldsymbol{\Omega}\boldsymbol{\Psi} - \boldsymbol{\Psi}\boldsymbol{\Omega} + 2\boldsymbol{B} - \frac{1}{\lambda_1}\boldsymbol{G}e^{-\boldsymbol{\Psi}} \tag{A.10}$$

This tensorial equation is discretized in time using a first order Euler scheme as:

$$\boldsymbol{\Psi}^{n} = \boldsymbol{\Psi}^{n-1} + \Delta t \left[-\mathbf{v} \cdot \nabla \boldsymbol{\Psi} + \boldsymbol{\Omega}\boldsymbol{\Psi} - \boldsymbol{\Psi}\boldsymbol{\Omega} + 2\boldsymbol{B} - \frac{1}{\lambda_1}\boldsymbol{G}e^{-\boldsymbol{\Psi}} \right]^{n-1} \tag{A.11}$$

By having the new values of $\boldsymbol{\Psi}$, the new value of conformation tensor $\mathbf{c}$ can be recovered by matrix-exponential operator of $\boldsymbol{\Psi}$ as:

$$\boldsymbol{c} = e^{\boldsymbol{\Psi}} \tag{A.12}$$

It is important to note that matrix-logarithm and matrix-exponential operators used in this section are tensor operators where the logarithm and the exponents are applied to the eigenvalues of the tensor.

Appendix B. Singularities of non-Viscoelastic regions: A droplet in shear test case

A two-dimensional test case of a viscoelastic/Newtonian droplet suspended in a Newtonian/viscoelastic matrix, all imposed to a simple shear flow is being solved using two different approaches of SAM and cut-off as described in section 3.3. This test case is being solved to make sure of the accuracy of applying a cut-off parameter to the relaxation time at the interface of viscoelastic/Newtonian interfaces for dealing with singularities of constitutive equation in Newtonian regions. The simulations of this section are similar to the cases of section 4.4. The results extracted with both SAM and cut-off approaches are compared with the benchmark results of Chinyoka et al. [72]. Computations have been performed using both structured and unstructured meshes with the edge size of h. All the simulations details are the same as described in section 4.4, except that here a 2D domain is used in discretization. In all these simulations the value of β is equal to 0.5 meaning equal shares of polymeric and solvent parts in viscoelastic fluid.

We perform four cases of dNmN, dVmN, dNmV, dVmV, in which **d** and **m** stand for droplet and matrix, and **N** and **V** stand for Newtonian and Viscoelastic, respectively. With this explanation, for example the phrase dVmN stands for a viscoelastic droplet suspended in Newtonian matrix.

Table B.6: Taylor deformation parameter (D) and inclination angle of the droplet (θ) for cases with different rheological properties solved with two approaches of (a) SAM and (b) cut-off, compared with the reference (ref) results of Chinyoka et al. [72].

Case	D_a	θ_a	D_b	θ_b	D_{ref}	θ_{ref}
dNmN	0.76	14.1	0.76	14.0	0.77	14.8
dVmN	0.71	15.2	0.71	15.3	0.72	15.7
dNmV	0.60	13.5	0.60	13.6	0.60	14.7
dVmV	0.55	14.4	0.55	14.5	0.55	15.8

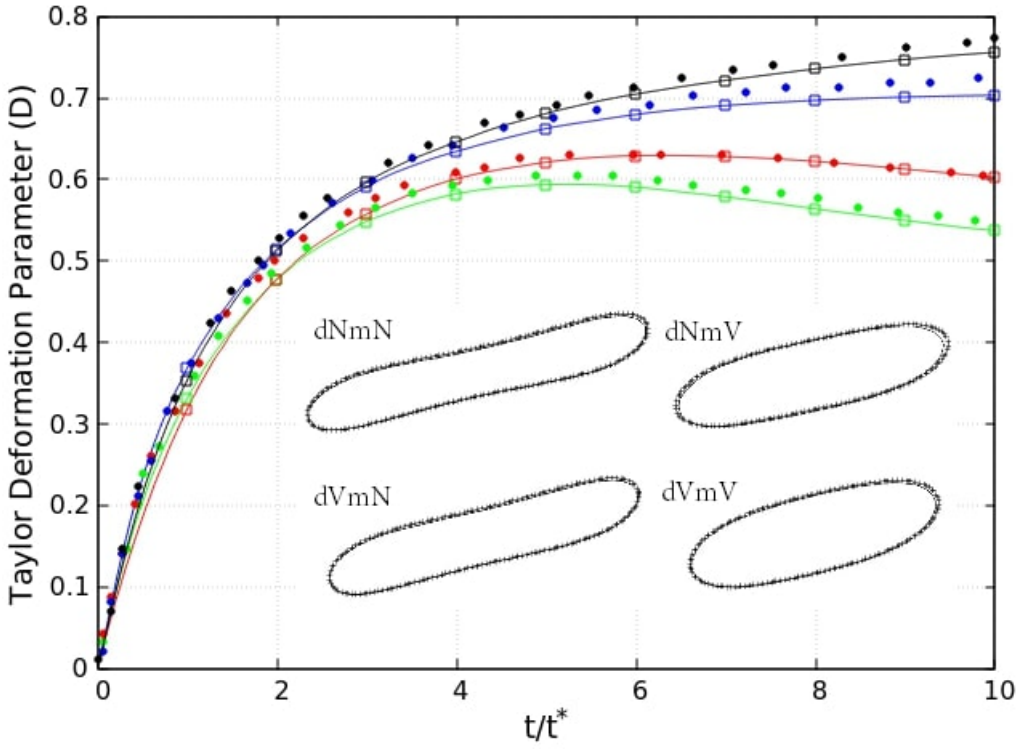

Figure B.19: Taylor deformation parameter (D) vs. time for cases with different rheologies properties all with Capillary number of 0.6, Reynolds number of 0.3, Deborah number of 0.4 and retardation ratio of 0.5. The colors black, blue, green, and red present the results for cases of dNmN, dVmN, dVmV and dNmV, respectively. The line results are related to the solution of the problem with cut-off approach, the square symbols are related to the solution of the problem with the SAM approach, and the circle symbols are related to the reference results of Chinyoka et al. [72]. The droplet shapes at steady-state are provided as well. In theses figures bold lines are reference figures of Chinyoka et al. [72] and points are results extracted in current study solved using cut-off approach.

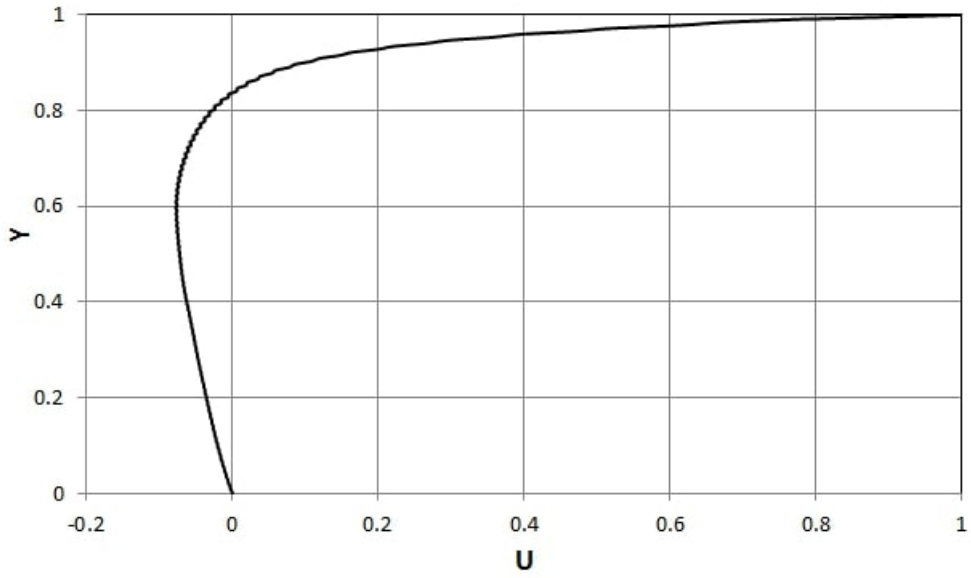

Figure C.20: Y(U) graph in the vertical centerlines of lid-driven cavity test case, with Re=100, for a viscoelastic fluid with viscosity ratio of $\beta = 0.0014$ and Weissenberg number equal to 0.75. For this test case, the predictor step of momentum equation is discretized using the Semi-Implicit form as eq. 22

.

In all of these cases, Capillary number of 0.6, Reynolds number of 0.3 and Deborah number of 0.4 are used. The simulations were run until t=10$\dot{\gamma}$. Figure B.19 presents the time variation of Taylor deformation parameter for solutions done in the current study using different approaches of SAM and cut-off, compared with the finite-difference/volume-of-fluid results of [72]. The steady-state droplet shape for the case solved in the current study using cut-off approach compared with the reference shapes of [72] are provided in this figure as well. The quantitative values of these cases are provided in table B.6. According to these data, the cut-off approach provides results almost identical to the SAM approach. Both approaches are having good agreement with the reference data of [72].

Appendix C. Studying ability of different approaches on solving LVRP

The selected test case is a two-dimensional lid-driven cavity problem, with geometrical characteristics and boundary conditions identical to the viscoelastic test case solved in section Appendix D. The Reynolds number is equal to 100, the value of viscosity ratio is $\beta = 0.0014$ and Weissenberg number is equal to 0.75.

Different discretizations of predictor step of momentum equation in the context of fractional-step projection method are being tested which are presented in table C.7. In this table, in the BSD discretization method, the term $\mathbf{D}_{hk}(\mathbf{v})$ is equal to $\nabla_h.(\mu_k/\mu_s\tau_s)$ with μ_k recommended to be equal to μ_p.

Table C.7: Different discretizations of predictor step of momentum equation used to study the LVRP.

method	discretization
Forward Euler	$\frac{\rho\mathbf{v}^*-\rho^n\mathbf{v}^n}{\Delta t} = \mathbf{C}_h(\rho\mathbf{v}^n) + \mathbf{D}_{hs}(\mathbf{v}^n) + \mathbf{D}_{hp}^n(\mathbf{v}^{n-1})$
Backward Euler	$\frac{\rho\mathbf{v}^*-\rho^n\mathbf{v}^n}{\Delta t} = \mathbf{C}_h(\rho\mathbf{v}^*) + \mathbf{D}_{hs}(\mathbf{v}^*) + \mathbf{D}_{hp}^*(\mathbf{v}^n)$
2nd order Adams-Bashforth	$\frac{\rho v^*-\rho^n v^n}{\Delta t} = \frac{3}{2}\left(\mathbf{C}_h(\rho\mathbf{v}^n) + \mathbf{D}_{hs}(\mathbf{v}^n) + \mathbf{D}_{hp}^n(\mathbf{v}^{n-1})\right)$- $\frac{1}{2}\left(\mathbf{C}_h(\rho\mathbf{v}^{n-1}) + \mathbf{D}_{hs}(\mathbf{v}^{n-1}) + \mathbf{D}_{hp}^{n-1}(\mathbf{v}^{n-2})\right)$
BSD	$\frac{\rho\mathbf{v}^*-\rho^n\mathbf{v}^n}{\Delta t} = \mathbf{C}_h(\rho\mathbf{v}^*) + \mathbf{D}_{hs}(\mathbf{v}^*) + \mathbf{D}_{hp}(\mathbf{v}^n) + \mathbf{D}_{hk}(\mathbf{v}^*) - \mathbf{D}_{hk}(\mathbf{v}^n)$
Semi-Implicit form as eq. 22	$\frac{\rho\mathbf{v}^*-\rho^n\mathbf{v}^n}{\Delta t} = \frac{3}{2}(R_h^v)^n - \frac{1}{2}(R_h^v)^{n-1} + \frac{1}{2}\left(\mathbf{D}_{hs}(\mathbf{v}^*) + \mathbf{D}_{hs}(\mathbf{v}^n)\right) - \nabla_h p^n$

The mentioned test case of two-dimensional lid-driven cavity with the predictor step of momentum equation being discretized according to the methods of table C.7 was solved for a long enough time of $t' = 10$ with $t' = t(U/D)$. An uniform structured square mesh with the edge size of $h = L/100$ was used in all the cases. Among all these methods tested, only the last method (Semi-Implicit form as eq. 22) was able to provide a stable solution for the aforementioned problem. The solution of methods of **Forward Euler** and **2nd order Adams-Bashforth** had an unbearably small timestep (around 5 orders of magnitude smaller than the other methods). With this small timestep, the solution process took a very long time to advance, however, for both of these methods the solution diverged for $t' \approx 1.2$. **Backward Euler** method didn't suffer from the significantly small timesteps as the two previous methods, however it failed to provide a solution and diverged at $t' \approx 3$. **BSD** method could benefit from timesteps as big as $dt' = 10^{-3}$. However this method also ended-up in diverging the solution process at $t' \approx 4.2$. Semi-Implicit form as eq. 22 was able to provide a stable solution using a constant timestep of $dt' = 10^{-3}$. The solution was successfully finished by the time $t' = 10$. Figure C.20 illustrates the Y(U) graph in the vertical centerlines of the geometry at time $t' = 10$ for this solution.

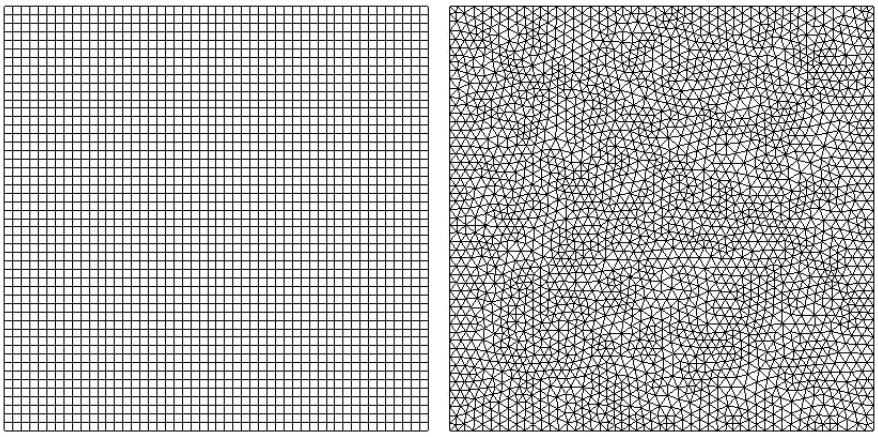

Figure D.21: Structured and Unstructured mesh configurations used in simulation of lid-driven cavity test case.

Appendix D. Additional tests: Lid-Driven Cavity

In this section, the results regarding the flow in classical two-dimensional lid-driven cavity test case will be presented. The lid-driven cavity problem has long been used as a validation case for new codes or new solution methods. This problem is of particular interest for testing for several reasons. There are many data available extracted from different experimental studies and numerical methods. The laminar solution of the flow is steady. Also, the geometry of problem is simple and two-dimensional, boundary conditions are simple and easy to implement. Numerical tests of this section are carried out on a benchmark problem studied in Carmona et al. [91], for GNFs and two different benchmark results of Chen et al. [62] and Yapici et al. [92] for viscoelastic fluids. The test case is a 2-D lid-driven cavity with aspect ratio of 1, characteristic length of L and characteristic velocity of $U = 1$. The top boundary of the cavity is moving with a velocity of u(x,t) while no-slip boundary condition is applied on other walls. Two different mesh types of structured and unstructured with a grid size of $h = L/100$ are used to discretize the solution domain as illustrated in figure D.21. The simulations are done for a long enough time to make sure that convergence to the steady-state has been reached. Three different sets of simulations are done for rheologies of viscoelastic, shear-thinning and shear-thickening fluids:

- For the case with viscoelastic fluid, Oldroyd-B constitutive equation is used. Three different formu-

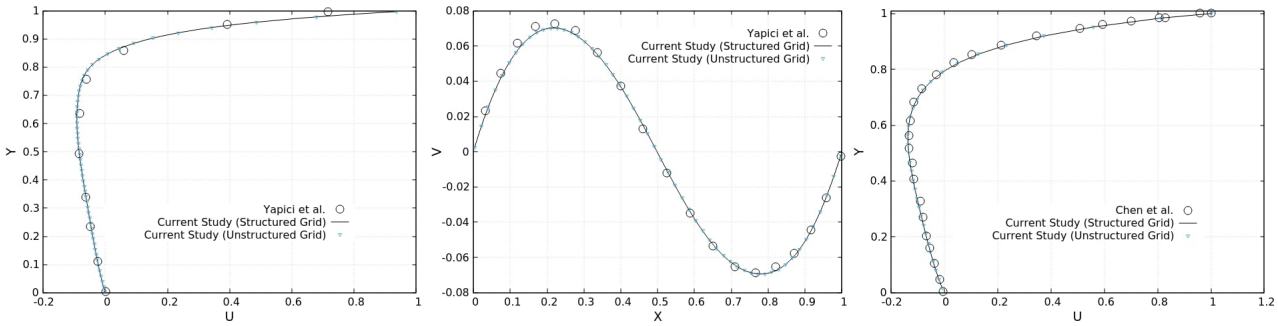

Figure D.22: Left and middle: Y(U) and V(X) graphs in the vertical and horizontal centerlines, respectively, for the lid-driven cavity problem, Case A compared with results of Yapici et al. [92].
Right: Y(U) graph in the vertical centerline of the lid-driven cavity problem, Case B compared with the results of Chen et al. [62].

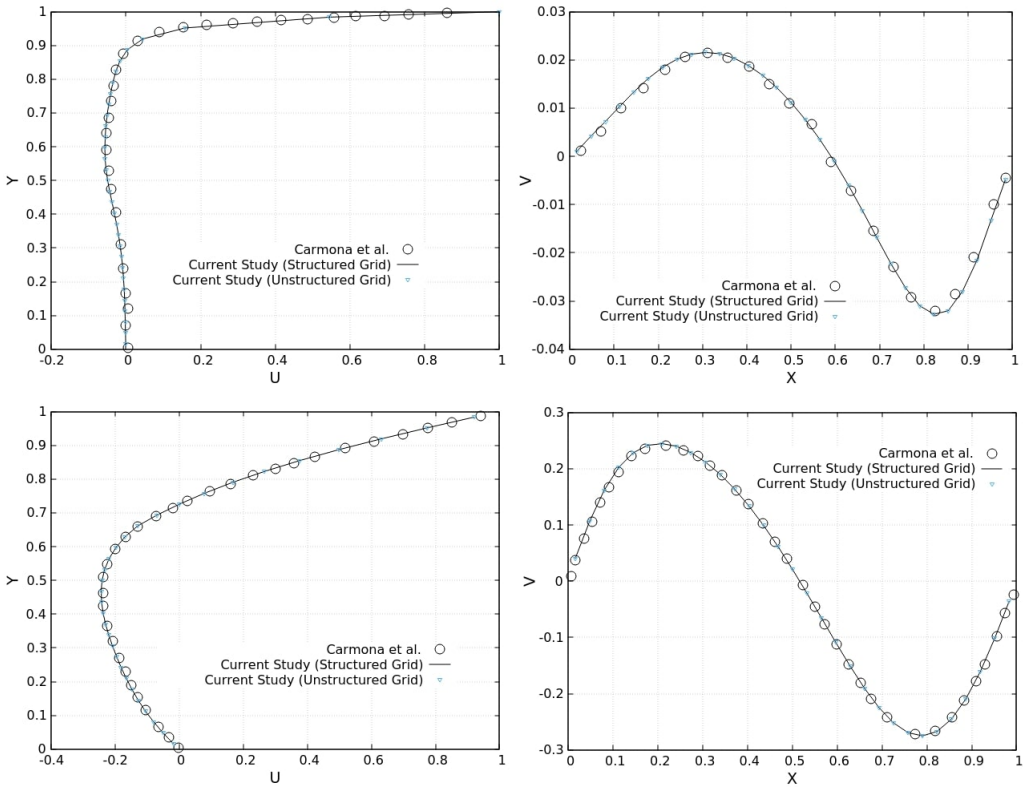

Figure D.23: Y(U) and V(X) graphs in the vertical and horizontal centerlines, respectively, for the lid-driven cavity problem with shear-thinning and shear-thickening fluids. First row corresponds to Case C (n=0.25) and second row corresponds to Case D (n=1.75). These graphs are compared with the results of Carmona et al. [91]

lations of Standard formulation, Log-Conformation Representation and semi analytical approaches of constitutive equation are used to verify the accuracy of the solver for this problem. Non-dimensional parameters of Reynolds number and Weissenberg number are defined as $Re = \rho UL/\mu_0$ and $Wi = \lambda_1 U/L$, respectively. In order to eliminate the singularities at the corners, the top wall moves with the space and time-dependent velocity profile as below:

$$u(x,t) = 8[1 + tanh(8t - 4)]x^2(1 - x^2) \tag{D.1}$$

The lid velocity gradually increases until it reaches its maximum magnitude at the center of the lid. In order to gain more confidence on the accuracy of the viscoelastic solver, two cases are selected and solved with different parameters of Re, Wi, and β in both structured and unstructured domains as:

Case A: Re=100, Wi=0.7 and β=0.3

Case B: Re=0.10, Wi=0.5 and β=0.5

The results are obtained for these cases in domains with structured and unstructured grids are compared with two different benchmarks of Chen et al. [62] and Yapici et al. [92], for cases A and B, respectively. Figure D.22 left and middle, represents the Y(U) and V(X) graphs in the vertical and horizontal centerlines of the domain, respectively. Figure D.22 right, however, represents Y(U) graph in the vertical centerline of the domain. The results of this figure correspond to the solution of viscoelastic fluid employing the Standard Formulation approach. The results of solution of these cases using LCR and SAM approaches are identical to the presented results. Hence, in order to avoid redundancy, these results are not added.

- In order to validate the ability of solver in capturing the physics of shear-thinning and shear-thickening fluids, simulations of generalized newtonian fluid represented with power-law model with two indices of n=0.25 (as shear-thinning fluid) and n=1.75 (as shear-thickening fluid) are performed:

Case C: Re=100, n=0.25

Case D: Re=100, n=1.75

Top wall is moving with a constant velocity of u(x,t)=1. Reynolds number is defined as $Re = \rho UL/K$ Figure D.23 represents the Y(U) and V(X) graphs in the vertical and horizontal centerlines of the domain extracted from solution in structured and unstructured grids, compared with results of Carmona et al. [91].

In all the cases presented in this section, a very good agreement is seen between the results extracted in this study, and the extracted data from literature.

References

[1] R. P. Chhabra, J. F. Richardson, Non-Newtonian flow in the process industries : fundamentals and engineering applications (1999) xiii, 436.

[2] R. B. Bird, C. F. Curtiss, R. C. Armstrong, O. Hassager, Dynamics of Polymeric Liquids, Kinetic Theory (Dynamics of Polymer Liquids Vol. 2) (Volume 2), volume 2 ed., Wiley-Interscience, 1987. URL: http://www.worldcat.org/isbn/0471802441.

[3] P. N. B. Reis, J. A. M. Ferreira, P. Santos, M. O. W. Richardson, J. B. Santos, Impact response of Kevlar composites with filled epoxy matrix, Composite Structures 94 (2012) 3520–3528.

[4] A. Majumdar, B. S. Butola, A. Srivastava, Development of soft composite materials with improved impact resistance using Kevlar fabric and nano-silica based shear thickening fluid, Materials & Design (1980-2015) 54 (2014) 295–300.

[5] O. E. Petel, S. Ouellet, J. Loiseau, D. L. Frost, A. J. Higgins, A comparison of the ballistic performance of shear thickening fluids based on particle strength and volume fraction, International Journal of Impact Engineering 85 (2015) 83–96.

[6] F. Irgens, Rheology and non-newtonian fluids, volume 9783319010, 2013. doi:10.1007/978-3-319-01053-3.

[7] L. Tassi, Chapter 5 - Kinematic viscosity and viscous flow in binary mixtures containing ethane-1,2-diol, in: N. P. Cheremisinoff (Ed.), Advances in Engineering Fluid Mechanics: Multiphase Reactor and Polymerization System Hydrodynamics, Gulf Professional Publishing, Burlington, 1996, pp. 79–104. URL: http://www.sciencedirect.com/science/article/pii/B9780884154976500073. doi:https://doi.org/10.1016/B978-088415497-6/50007-3.

[8] A. Bansal, R. K. Wanchoo, S. K. Sharma, Two-phase pressure drop in a trickle bed reactor involving newtonian/ non-newtonian liquid phase, Chemical Engineering Communications 195 (2008) 1085–1106.

[9] M. F. Tomé, N. Mangiavacchi, J. A. Cuminato, A. Castelo, S. McKee, A finite difference technique for simulating unsteady viscoelastic free surface flows, Journal of Non-Newtonian Fluid Mechanics 106 (2002) 61–106.

[10] C. M. Oishi, F. P. Martins, M. F. Tomé, M. A. Alves, Numerical simulation of drop impact and jet buckling problems using the eXtended Pom-Pom model, Journal of Non-Newtonian Fluid Mechanics 169-170 (2012) 91–103.

[11] M. F. Tome, S. McKee, Numerical simulation of viscous flow: Buckling of planar jets, International Journal for Numerical Methods in Fluids 29 (1999) 705–718.

[12] S. McKee, M. F. Tomé, V. G. Ferreira, J. A. Cuminato, A. Castelo, F. S. Sousa, N. Mangiavacchi, The MAC method, Computers and Fluids 37 (2008) 907–930.

[13] S. Mukherjee, K. Sarkar, Effects of viscoelasticity on the retraction of a sheared drop, Journal of Non-Newtonian Fluid Mechanics 165 (2010) 340–349.

[14] S. Mukherjee, K. Sarkar, Effects of viscosity ratio on deformation of a viscoelastic drop in a Newtonian matrix under steady shear, Journal of Non-Newtonian Fluid Mechanics (2009).

[15] L. S. Ferreira, J. O. Trierweiler, Modeling and simulation of the polymeric nanocapsule formation process, IFAC Proceedings Volumes (IFAC-PapersOnline) 7 (2009) 405–410.

[16] N. Aggarwal, K. Sarkar, Effects of matrix viscoelasticity on viscous and viscoelastic drop deformation in a shear flow, Journal of Fluid Mechanics 601 (2008) 63–84.

[17] D. Izbassarov, M. Muradoglu, A computational study of two-phase viscoelastic systems in a capillary tube with a sudden contraction/expansion Viscoelastic effects on drop deformation in a converging pipe flow A computational study of two-phase viscoelastic systems in a capillary tube, Physics of Fluids Fluids Fluids J. Rheol. Phys. Fluids 28 (2016) 12110–92001.

[18] N. G. Deen, M. v. S. Annaland, J. A. Kuipers, Direct numerical simulation of complex multi-fluid flows using a combined front tracking and immersed boundary method, Chemical Engineering Science (2009).

[19] J. Fang, R. G. Owens, L. Tacher, A. Parriaux, A numerical study of the SPH method for simulating transient viscoelastic free surface flows, Journal of Non-Newtonian Fluid Mechanics 139 (2006) 68–84.

[20] T. Jiang, J. Ouyang, B. Yang, J. Ren, The SPH method for simulating a viscoelastic drop impact and spreading on an inclined plate, Computational Mechanics 45 (2010) 573–583.

[21] A. Rafiee, M. T. Manzari, M. Hosseini, An incompressible SPH method for simulation of unsteady viscoelastic free-surface flows, International Journal of Non-Linear Mechanics 42 (2007) 1210–1223.

[22] A. Zainali, N. Tofighi, M. S. Shadloo, M. Yildiz, Numerical investigation of Newtonian and non-Newtonian multiphase flows using ISPH method, Computer Methods in Applied Mechanics and Engineering 254 (2013) 99–113.

[23] A. J. Wagner, L. Giraud, C. E. Scott, Simulation of a cusped bubble rising in a viscoelastic fluid with a new numerical method, Computer Physics Communications 129 (2000) 227–232.

[24] X. Frank, J.-C. Charpentier, Y. Ma, N. E. Midoux, H. Z. Li, A Multiscale Approach for Modeling Bubbles Rising in Non-Newtonian Fluids, Ind. Eng. Chem. Res 51 (2012) 2084–2093.

[25] N. Wang, H. Liu, C. Zhang, Deformation and breakup of a confined droplet in shear flows with power-law rheology,

Journal of Rheology 61 (2017) 741–758.

[26] A. Gupta, M. Sbragaglia, Deformation and break-up of Viscoelastic Droplets Using Lattice Boltzmann Models, in: Procedia IUTAM, volume 15, 2015, pp. 215–227. URL: www.sciencedirect.com. doi:10.1016/j.piutam.2015.04.030.

[27] K. Sun, T. Wang, P. Zhang, C. K. Law, Non-Newtonian flow effects on the coalescence and mixing of initially stationary droplets of shear-thinning fluids, Physical Review E - Statistical, Nonlinear, and Soft Matter Physics 91 (2015) 1–10.

[28] C. Xie, J. Zhang, V. Bertola, M. Wang, Lattice Boltzmann modeling for multiphase viscoplastic fluid flow, Journal of Non-Newtonian Fluid Mechanics 234 (2016) 118–128.

[29] J. Y. Shao, C. Shu, H. B. Huang, Y. T. Chew, Free-energy-based lattice Boltzmann model for the simulation of multiphase flows with density contrast, Physical Review E - Statistical, Nonlinear, and Soft Matter Physics (2014).

[30] S. Zou, X.-F. Yuan, X. Yang, W. Yi, X. Xu, An integrated lattice Boltzmann and finite volume method for the simulation of viscoelastic fluid flows, Journal of Non-Newtonian Fluid Mechanics 211 (2014) 99–113.

[31] S. F. Lunkad, V. V. Buwa, K. D. Nigam, Numerical simulations of drop impact and spreading on horizontal and inclined surfaces, Chemical Engineering Science 62 (2007) 7214–7224.

[32] J. L. Favero, A. R. Secchi, N. S. M. Cardozo, H. Jasak, Viscoelastic fluid analysis in internal and in free surface flows using the software OpenFOAM, Computers and Chemical Engineering 34 (2010) 1984–1993.

[33] A. Bonito, M. Picasso, M. Laso, Numerical simulation of 3D viscoelastic flows with free surfaces POOPING, Journal of Computational Physics 215 (2006) 691–716.

[34] W. Sun, C. Zhu, T. Fu, H. Yang, Y. Ma, H. Li, The minimum in-line coalescence height of bubbles in non-Newtonian fluid, International Journal of Multiphase Flow 92 (2017) 161–170.

[35] A. Torkkeli, Droplet microfluidics on a planar surface, VTT Publications 61 (2003) 3–194.

[36] N. O. Moraga, L. A. Lemus, M. A. Saavedra, R. A. Lemus-Mondaca, VOF/FVM prediction and experimental validation for shear-thinning fluid column collapse, Computers and Mathematics with Applications 69 (2015) 89–100.

[37] B. P. Leonard, The ULTIMATE conservative difference scheme applied to unsteady one-dimensional advection, Computer Methods in Applied Mechanics and Engineering 88 (1991) 17–74.

[38] A. R. Premlata, M. Kumar, B. Karri, K. Chandra, Dynamics of an air bubble rising in a non-Newtonian liquid in the axisymmetric regime, Journal of Non-Newtonian Fluid Mechanics 239 (2017) 53–61.

[39] C. Focke, D. Bothe, Direct numerical simulation of binary off-center collisions of shear thinning droplets at high Weber numbers, Physics of Fluids 24 (2012).

[40] S. Abishek, A. J. King, R. Narayanaswamy, Dynamics of a Taylor bubble in steady and pulsatile co-current flow of Newtonian and shear-thinning liquids in a vertical tube, International Journal of Multiphase Flow 74 (2015) 148–164.

[41] J. D. Araújo, J. M. Miranda, J. B. Campos, Taylor bubbles rising through flowing non-Newtonian inelastic fluids, Journal of Non-Newtonian Fluid Mechanics 245 (2017) 49–66.

[42] R. Figueiredo, C. Oishi, A. Afonso, I. Tasso, J. Cuminato, A two-phase solver for complex fluids: Studies of the Weissenberg

effect, International Journal of Multiphase Flow 84 (2016) 98–115.

[43] J. M. López-Herrera, S. Popinet, A. A. Castrejón-Pita, An adaptive solver for viscoelastic incompressible two-phase problems applied to the study of the splashing of weakly viscoelastic droplets, Journal of Non-Newtonian Fluid Mechanics 264 (2019) 144–158.

[44] M. Sussman, E. G. Puckett, A Coupled Level Set and Volume-of-Fluid Method for Computing 3D and Axisymmetric Incompressible Two-Phase Flows, Journal of Computational Physics (2000).

[45] J. D. Yu, S. Sakai, J. A. Sethian, Two-phase viscoelastic jetting, Journal of Computational Physics 220 (2007) 568–585.

[46] T. E. Tezduyar, S. Sathe, M. Schwaab, B. S. Conklin, Convected level set method for the numerical simulation of fluid buckling, International Journal for Numerical Methods in Fluids (2008) 601–629.

[47] J. L. Prieto, Stochastic particle level set simulations of buoyancy-driven droplets in non-Newtonian fluids, Journal of Non-Newtonian Fluid Mechanics 226 (2015) 16–31.

[48] S. B. Pillapakkam, P. Singh, D. Blackmore, N. Aubry, Transient and steady state of a rising bubble in a viscoelastic fluid, Journal of Fluid Mechanics 589 (2007) 215–252.

[49] E. Olsson, G. Kreiss, A conservative level set method for two phase flow, Journal of Computational Physics 210 (2005) 225–246.

[50] N. Balcazar, L. Jofre, O. Lehmkuhl, J. Castro, J. Rigola, A finite-volume/level-set method for simulating two-phase flows on unstructured grids, International Journal of Multiphase Flow 64 (2014) 55–72.

[51] N. Balcázar, O. Lehmkuhl, L. Jofre, J. Rigola, A. Oliva, A coupled volume-of-fluid/level-set method for simulation of two-phase flows on unstructured meshes, Computers & Fluids 124 (2016) 12–29.

[52] A. Amani, N. Balcázar, E. Gutiérrez, A. Oliva, Numerical study of binary droplets collision in the main collision regimes, Chemical Engineering Journal (2019) 477–498.

[53] A. Amani, N. Balcázar, J. Castro, A. Oliva, Numerical study of droplet deformation in shear flow using a conservative level-set method, Chemical Engineering Science 207 (2019) 153–171.

[54] A. Amani, N. Balcazar, A. Naseri, A. Oliva, A Study on Binary Collision of GNF Droplets Using a Conservative Level-Set Method, in: 6th European Conference on Computational Mechanics (ECCM 6)- 7th European Conference on Computational Fluid Dynamics (ECFD 7), Glasgow, UK, 2018.

[55] E. Olsson, G. Kreiss, A conservative level set method for two phase flow, Journal of Computational Physics 210 (2005) 225–246.

[56] N. Balcázar, O. Lehmkuhl, J. Rigola, A. Oliva, A multiple marker level-set method for simulation of deformable fluid particles, International Journal of Multiphase Flow 74 (2015) 125–142.

[57] J. U. Brackbill, D. B. Kothe, C. Zemach, A continuum method for modeling surface tension, Journal of Computational Physics 100 (1992) 335–354.

[58] A. J. Chorin, Numerical solution of the Navier-Stokes equations, Mathematics of Computation 22 (1968) 745–745.

[59] S. Armfield, R. Street, An analysis and comparison of the time accuracy of fractional-step methods for the Navier-Stokes equations on staggered grids, International Journal for Numerical Methods in Fluids 38 (2002) 255–282.

[60] N. Balcázar-Arciniega, O. Antepara, J. Rigola, A. Oliva, A level-set model for mass transfer in bubbly flows, International Journal of Heat and Mass Transfer 138 (2019) 335–356.

[61] A. S. Almgren, J. B. Bell, P. Colella, L. H. Howell, M. L. Welcome, A Conservative Adaptive Projection Method for the Variable Density Incompressible Navier-Stokes Equations, Journal of Computational Physics 142 (1998) 1–46.

[62] X. Chen, H. Marschall, M. Schäfer, D. Bothe, A comparison of stabilisation approaches for finite-volume simulation of viscoelastic fluid flow, International Journal of Computational Fluid Dynamics 27 (2013) 229–250.

[63] R. Fattal, R. Kupferman, Constitutive laws for the matrix-logarithm of the conformation tensor, Journal of Non-Newtonian Fluid Mechanics 123 (2004) 281–285.

[64] M. A. Hulsen, A. P. G. van Heel, B. van den Brule, Simulation of viscoelastic flows using Brownian configuration fields, Journal of Non-Newtonian Fluid Mechanics 70 (1997) 79–101.

[65] J. Lee, S. Yoon, Y. Kwon, S. Kim, Practical comparison of differential viscoelastic constitutive equations in finite element analysis of planar 4:1 contraction flow, Rheologica Acta 44 (2004) 188–197.

[66] M. Renardy, Current issues in non-Newtonian flows: A mathematical perspective, Journal of Non-Newtonian Fluid Mechanics 90 (2000) 243–259.

[67] R. Fattal, R. Kupferman, Time-dependent simulation of viscoelastic flows at high Weissenberg number using the log-conformation representation, Journal of Non-Newtonian Fluid Mechanics 126 (2005) 23–37.

[68] M. A. Hulsen, R. Fattal, R. Kupferman, Flow of viscoelastic fluids past a cylinder at high Weissenberg number: Stabilized simulations using matrix logarithms, Journal of Non-Newtonian Fluid Mechanics 127 (2005) 27–39.

[69] P. A. Stewart, N. Lay, M. Sussman, M. Ohta, An improved sharp interface method for viscoelastic and viscous two-phase flows, Journal of Scientific Computing 35 (2008) 43–61.

[70] N. Balci, B. Thomases, M. Renardy, C. R. Doering, Symmetric factorization of the conformation tensor in viscoelastic fluid models, Journal of Non-Newtonian Fluid Mechanics 166 (2011) 546–553.

[71] K. Sarkar, W. R. Schowalter, Deformation of a two-dimensional viscoelastic drop at non-zero Reynolds number in time-periodic extensional flows, Journal of Non-Newtonian Fluid Mechanics 95 (2000) 315–342.

[72] T. Chinyoka, Y. Y. Renardy, M. Renardy, D. B. Khismatullin, Two-dimensional study of drop deformation under simple shear for Oldroyd-B liquids, Journal of Non-Newtonian Fluid Mechanics 130 (2005) 45–56.

[73] L. J. Amoreira, P. J. Oliveira, Comparison of different formulations for the numerical calculation of unsteady incompressible viscoelastic fluid flow, Advances in Applied Mathematics and Mechanics 2 (2010) 483–502.

[74] S. Gottlieb, C.-W. Shu, Total variation diminishing Runge-Kutta schemes, Mathematics of computation of the American Mathematical Society 67 (1998) 73–85.

[75] N. Balcázar, L. Jofre, O. Lehmkuhl, J. Castro, J. Rigola, A finite-volume/level-set method for simulating two-phase flows

on unstructured grids, International Journal of Multiphase Flow 64 (2014) 55–72.

[76] C. M. Rhie, W. L. Chow, Numerical study of the turbulent flow past an airfoil with trailing edge separation, AIAA journal 21 (1983) 1525–1532.

[77] F. N. Felten, T. S. Lund, Kinetic energy conservation issues associated with the collocated mesh scheme for incompressible flow, Journal of Computational Physics 215 (2006) 465–484.

[78] N. Balcázar, J. Rigola, J. Castro, A. Oliva, A level-set model for thermocapillary motion of deformable fluid particles, International Journal of Heat and Fluid Flow 0 (2016) 1–20.

[79] Termo Fluids S.L., 0. URL: http://www.termofluids.com/.

[80] N. Balcázar, O. Lehmkuhl, L. Jofre, A. Oliva, Level-set simulations of buoyancy-driven motion of single and multiple bubbles, International Journal of Heat and Fluid Flow 56 (2015) 91–107.

[81] N. Balcázar, O. Lehmkuhl, L. Jofre, J. Rigola, A. Oliva, A coupled volume-of-fluid/level-set method for simulation of two-phase flows on unstructured meshes, Computers and Fluids 124 (2016) 12–29.

[82] E. Gutiérrez, F. Favre, N. Balcázar, A. Amani, J. Rigola, Numerical approach to study bubbles and drops evolving through complex geometries by using a level set-Moving mesh-Immersed boundary method, Chemical Engineering Journal 349 (2018) 662–682.

[83] A. Amani, N. Balcazar, E. Gutiérrez, A. Oliva, DNS of un-equal size droplets collision using a moving-mesh/level-set method, in: ERCOFTAC workshop direct and large eddy simulation 12 (DLES 12), Madrid, Spain, 2019.

[84] E. O. Carew, P. Townsend, M. F. Webster, Taylor-Galerkin algorithms for viscoelastic flow: Application to a model problem, Numerical Methods for Partial Differential Equations 10 (1994) 171–190.

[85] S. Popinet, Numerical Models of Surface Tension, Annual Review of Fluid Mechanics 50 (2018) 49–75.

[86] J. Luo, X. Y. Hu, N. A. Adams, Curvature boundary condition for a moving contact line, Journal of Computational Physics 310 (2016) 329–341.

[87] J. Venkatesan, S. Ganesan, Computational modeling of impinging viscoelastic droplets, Journal of Non-Newtonian Fluid Mechanics 263 (2019) 42–60.

[88] D. J. E. Harvie, J. J. Cooper-White, M. R. Davidson, Deformation of a viscoelastic droplet passing through a microfluidic contraction, Journal of Non-Newtonian Fluid Mechanics 155 (2008) 67–79.

[89] S. Guido, M. Simeone, F. Greco, Deformation of a Newtonian drop in a viscoelastic matrix under steady shear flow Experimental validation of slow flow theory, Journal of Non-Newtonian Fluid Mechanics 114 (2003) 65–82.

[90] P. L. Maffettone, F. Greco, Ellipsoidal drop model for single drop dynamics with non-Newtonian fluids, Journal of Rheology 48 (2004) 83–100.

[91] A. Carmona, O. Lehmkuhl, C. D. Pérez-Segarra, A. Oliva, Numerical analysis of the transpose diffusive term for viscoplastic-type non-newtonian fluid flows using a collocated variable arrangement, Numerical Heat Transfer, Part B: Fundamentals 67 (2015) 410–436.

[92] K. Yapici, B. Karasozen, Y. Uludag, Journal of Non-Newtonian Fluid Mechanics Finite volume simulation of viscoelastic laminar flow in a lid-driven cavity 164 (2009) 51–65.